Chemical Geology 334 (2012) 345–363

Contents lists available at SciVerse ScienceDirect

Chemical Geology

journal homepage: www.elsevier.com/locate/chemgeo

Speciation of nickel (II) chloride complexes in hydrothermal fluids: *In situ* XAS study

Yuan Tian [a,b], Barbara Etschmann [c], Weihua Liu [d], Stacey Borg [d,h], Yuan Mei [b,c,d], Denis Testemale [e], Brian O'Neill [a], Nick Rae [f], David M. Sherman [g], Yung Ngothai [a], Bernt Johannessen [i], Chris Glover [i], Joël Brugger [b,c,*]

[a] School of Chemical Engineering, The University of Adelaide, Adelaide 5000, South Australia, Australia
[b] Division of Mineralogy, South Australian Museum, Adelaide 5000, South Australia, Australia
[c] Tectonics, Resources and Exploration (TRaX), School of Earth and Environmental Sciences, The University of Adelaide, Adelaide 5000, South Australia, Australia
[d] CSIRO Earth Science and Resource Engineering, Clayton, Victoria 3168, Australia
[e] Institut Néel, CNRS et Université Joseph Fourier, BP 166, 38042 Grenoble Cédex 9, France and FAME beamline, ESRF, 38043 Grenoble, France
[f] School of Physics, The University of Melbourne, 3010 Parkville, Vic., Australia
[g] School of Earth Sciences, University of Bristol, Bristol BS8 1RJ, UK
[h] CODES ARC Centre of Excellence in Ore Deposits, University of Tasmania, Hobart, TAS 7001, Australia
[i] Australian Synchrotron, 800 Blackburn Road, Clayton, VIC 3168, Australia

ARTICLE INFO

Article history:
Received 8 April 2012
Received in revised form 1 October 2012
Accepted 3 October 2012
Available online 15 October 2012

Editor: J. Fein

Keywords:
X-ray absorption spectroscopy
Speciation
Ni(II) chloride complexes
Coordination change
ab initio XANES
Hydrothermal fluids

ABSTRACT

In situ XAS data of Ni(II) chloride solutions with various salinities (0–7.68 m) were collected to investigate the stoichiometry and geometry of Ni(II) chloride complexes from room temperature up to 369 °C at 400 bar, and to 434 °C at 600 bar. Increasing temperature and/or salinity results in a change in the coordination of the Ni(II) chlorocomplexes from octahedral to (distorted) tetrahedral. Octahedral species predominate within the whole salinity range at room temperature and up to ~200 °C, and tetrahedral species become significant beyond this temperature. At 369 °C and 400 bar, octahedral species remain in equilibrium with tetrahedral species, and the number of chloride ligands in the first coordination shell depends on the Cl:Ni molar ratio. EXAFS refinements and *ab initio* XANES calculations show that the highest order chlorocomplex present over the investigated pressure, temperature and composition ranges is the distorted tetrahedral complex $[NiCl_3(H_2O)]^-$, which predominates in the highest Cl concentration (7.68 m) solution at 434 °C and 600 bar. A quantitative thermodynamic analysis of the XANES and EXAFS data reveals that the XAS data are consistent with the speciation models derived from recent UV-Vis spectrophotometric measurements (25 °C–250 °C, 100 bar; Liu et al., 2012b) and the high temperature, high pressure solubility experiments of Lin and Popp (1984) and Fahlquist and Popp (1989), if the $NiCl_{2(aq)}$ species exists in both octahedral ($[NiCl_2(H_2O)_4]_{(aq)}$) and tetrahedral ($[NiCl_2(H_2O)_2]_{(aq)}$) forms, with the ratio of octahedral to tetrahedral decreasing at high temperature (>200 °C). The new XAS data show that the octahedral to tetrahedral transition in Ni(II) chloride complexes occurs at higher temperature and/or salinity than the corresponding Co(II) complexes (Liu et al., 2011).

1. Introduction

Nickel is currently mined from two main classes of deposits (Harald, 2010): magmatic sulfide deposits where Ni occurs in the form of sulfide minerals and metal enrichment is related to magmatic fractionation processes, in particular the formation of immiscible sulfide melts within mafic and ultramafic magmas (Barnes and Lightfoot, 2005); and lateritic Ni deposits, where Ni is hosted in phases such as nickeliferous limonite and garnierite, and that form as a result of chemical weathering of Ni-bearing ultramafic and mafic rocks in tropical and sub-tropical climates (Fan and Gerson, 2011). In the past decade, there has been growing evidence that many magmatic Ni deposits have been subjected to extensive hydrothermal alteration that resulted in changes in mineralogy and in local remobilization of the metals (Molnar et al., 2001; Ripley et al., 2005; Almeida et al., 2007; Barnes and Liu, 2012). In some cases, hydrothermal remobilization of Ni from mafic and ultramafic source rocks is thought to have been directly responsible for the formation of economic concentrations of Ni sulfides (*e.g.*, Avebury deposit, Tasmania, Australia; Keays et al., 2009). There are also a few hydrothermal vein deposits in which Ni is one of the metals, such as the five-metal veins in the Cobalt Mining Camp, Ontario, Canada (Kissin, 1992), and the Co–Ni–Bi veins in the Permian Kupferschiefer, Germany (Wagner and Lorenz, 2002).

Understanding Ni transport and deposition relies on our knowledge of the aqueous complexes responsible for the solubility of Ni in hydrothermal fluids and on the availability of thermodynamic properties for each of the relevant species as a function of pressure, temperature, and fluid chemistry (Seward and Barnes, 1997; Brugger et al., 2010;

* Corresponding author at: School of Earth and Environmental Sciences, The University of Adelaide, Adelaide 5000, South Australia, Australia.
E-mail address: joel.brugger@adelaide.edu.au (J. Brugger).

0009-2541/$ – see front matter © 2012 Elsevier B.V. All rights reserved.
http://dx.doi.org/10.1016/j.chemgeo.2012.10.010

Barnes and Liu, 2012). Hence, knowledge of Ni(II) speciation and of the thermodynamic properties of the significant complexes is required to improve predictive mineral exploration strategies and increase the efficiency of mineral and metallurgical processing techniques (*e.g.*, Seward and Driesner, 2004; Brugger et al., 2007). Since Ni and Co are geochemical 'twins' that occur in close association in nature, another motivation for this work is to compare the nature of Ni(II) chlorocomplexes with those of Co(II) chlorocomplexes recently characterized by X-ray Absorption Spectroscopy (XAS) (Liu et al., 2011) and solubility studies (Migdisov et al., 2011) in order to constrain the fractionation among these elements in hydrothermal systems.

A number of studies have been carried out to investigate Ni(II) aqueous speciation in a wide range of conditions using different techniques (Table 1). Several UV-Vis spectrophotometric studies investigated the effects of temperature, salinity and pressure on the structural transition of Ni-aqua-halo complexes in brines up to 400 °C (Angell and Gruen, 1966; Lüdemann and Franck, 1967, 1968; Susak and Crerar, 1985; Suleimenov, 2004; see Table 1). These qualitative studies identified the octahedral to tetrahedral transition of Ni(II) halide complexes at high temperature and listed possible species present. Most of these studies highlighted the importance of high order tetrahedral complex (*e.g.*, $[NiCl_3(H_2O)]^-$ and/or $[NiCl_4]^{2-}$) at high temperature and high salinity, but did not provide quantitative thermodynamic analysis for the proposed species. A recent UV-Vis study (26–250 °C, 100 bar) by Liu et al. (2012b) reports thermodynamic properties for Ni(II) chlorocomplexes, and concludes that Ni^{2+}, $NiCl^+$ and $NiCl_{2(aq)}$ are the dominant species up to 250 °C, with small amounts of $NiCl_3^-$ present above 150 °C at high salt concentrations (experiments conducted up to 3 m Cl_{tot}). At higher temperatures and pressures, the formation constants of $NiCl_{2(aq)}$ (450–700 °C, 1–2 kbar; Ni:Cl molar ratio > 1:3; Lin and Popp, 1984) and $NiCl_3^-$ (550–750 °C, 2 kbar; NaCl concentrations up to 6.5 m; Fahlquist and Popp, 1989; Uchida et al., 1996) were derived from measurements of the solubility of $NiO_{(s)}$. Hydrolysis constants of Ni(II) hydroxo-complexes were also derived from solubility measurements (Tremaine and Leblanc, 1980; Ziemniak and Goyette, 2004; Palmer et al., 2011). The most recent study of hydroxide complexing suggests that a single species, $Ni(OH)_{2(aq)}$, dominates Ni speciation in basic solutions over the temperature range 25 °C to 350 °C (Palmer et al., 2011). Using a combination of XAS, near-infrared spectroscopy, and classical Molecular Dynamics (MD), Wallen et al. (1998) and Hoffmann et al. (1999) provided a molecular-level analysis (coordination number, bond length, and complex geometry) of the structural transition of Ni(II) bromide complexes from octahedral at ambient temperature to distorted tetrahedral up to supercritical conditions (25–525 °C, 1–720 bar, up to 1.2 m Br_{tot}). The highest order complex characterized by Hoffmann et al. (1999) was $[NiBr_3(H_2O)]^-$. However, there is currently no quantitative study, in particular no XAS data, on the geometry of the Ni(II) chlorocomplexes, despite that chloride is one of the most common ligands in hydrothermal ore fluid (Seward and Barnes, 1997).

In this study we used a combination of XAS experiments, *ab initio* X-ray Absorption Near Edge Structure (XANES) and Extended X-ray Absorption Fine Structure (EXAFS) calculations, and Density Functional Theory (DFT) calculations to provide a molecular-level understanding of Ni(II) chloride complexing in acidic solutions under a wide range of conditions (25–434 °C, 400–600 bar, $0 < Cl_{tot} < 7.68$ m). The aims of this study include: i) constrain the nature (stoichiometry and geometry) of Ni(II)-aqua-chloro complexes at elevated temperatures and pressures using EXAFS and XANES; ii) map the effects of temperature and salinity on the coordination changes of Ni(II)-aqua-chloro complexes; and iii) assess the consistency of the new structural information with the predictions from the thermodynamic model for Ni(II) speciation in chloride brines derived by Liu et al. (2012b) on the basis of UV-Vis data (to 250 °C) as well as on the high PT solubility data of Fahlquist and Popp (1989), Lin and Popp (1984) and Uchida et al. (1996). Overall, this study aims to improve our ability to model Ni mobility under hydrothermal conditions.

2. Materials and measurements

All chemicals were purchased from Sigma-Aldrich and were of analytical grade (NaCl, LiCl, $NiSO_4 \cdot 6H_2O_{(s)}$ and $NiCl_2.6H_2O_{(s)}$ with purity > 98%; $NiO_{(s)}$ with purity > 99.8%). $NiO_{(s)}$, $NiSO_4 \cdot 6H_2O_{(s)}$ and $NiCl_2 \cdot 6H_2O_{(s)}$ were also used as standards for XAS, together with the following Ni minerals from the collections of the South Australian Museum (gaspeite — South Australian Museum collection number G12242; vaesite — G6176; heazlewoodite — G27737; polydymite — G549; violarite — G5633; pentlandite — G487). The identity of the mineral phases was checked by powder X-ray diffraction. The Ni stock solutions were prepared by dissolving $NiCl_2 \cdot 6H_2O_{(s)}$ in Millipore® doubly deionized water, and slightly acidified with HCl to prevent hydrolysis of Ni^{2+} (0.06 m and 0.03 m HCl added for the preparation of NaCl and LiCl solutions, respectively). We used the HCh program (Shvarov and Bastrakov, 1999) to calculate the high temperature pH, and to confirm that Ni(II) hydroxide complexes (properties from Palmer et al., 2011) are not significant (≪1%) and can be ignored. Different amounts of NaCl were added to control the salinity of each

Table 1
Previous studies on aqueous Ni(II) halide and hydroxide complexes under hydrothermal conditions.

Method	T, P and salinity range	Species identified	Reference
Chloride and bromide complexes			
UV-Vis spectrophotometry	25–320 °C, P_{sat}, 0 m ≤ mCl ≤ 22 m	Octahedral(O_h) Ni–Cl–(H_2O) species[a] Tetrahedral(T_d) Ni–Cl–(H_2O) species[b]	Angell and Gruen (1966)
UV-Vis spectrophotometry	25–300 °C, 0.5/6 kbar, 0.025 m $NiBr_2$	$Ni(H_2O)_6^{2+}$	Lüdemann and Franck (1967)
UV-Vis spectrophotometry	25–350 °C, 0.5/6 kbar, 4 m ≤ mCl ≤ 10 m	$NiCl_2(H_2O)_{2(aq)}$, $NiCl_3(H_2O)^-$	Lüdemann and Franck (1968)
UV-Vis spectrophotometry	25–300 °C, P_{sat}, mCl ≤ 5 m	O_h Ni–Cl–(H_2O) species [a] T_d $NiCl(H_2O)_3^+$	Susak and Crerar (1985)
UV-Vis spectrophotometry	20–400 °C, 0.1–0.9 kbar, 0.1 m $NiCl_2$	$Ni(H_2O)_6^{2+}$, T_d Ni–Cl–(H_2O) species	Suleimenov (2004)
UV-Vis spectrophotometry	26–250 °C, 0.1 kbar, mCl ≤ 3 m	$NiCl^+$, $NiCl_{2(aq)}$, $NiCl_3^-$	Liu et al. (2012b)
Solubility	450–700 °C, 1–2 kbar, mCl ≤ 0.1 m	$NiCl_{2(aq)}$	Lin and Popp (1984)
Solubility	550–750 °C, 2 kbar, mCl ≤ 6.5 m	$NiCl_3^-$	Fahlquist and Popp (1989)
Solubility	600 °C, 1 kbar, mCl ≤ 1.6 mol/L	$NiCl_{2(aq)}$, $NiCl_3^-$	Uchida et al. (1996)
Neutron Diffraction	100 °C and 300 °C, 1 kbar, 2 m $NiCl_2$	$Ni(H_2O)_6^{2+}$, $Ni(H_2O)_5^{2+}$, $Ni(H_2O)_4^{2+}$	Jong et al., (1996)
XAS and MD	25–425 °C, 1–690 bar, 0.4 m ≤ mBr ≤ 0.8 m	$Ni(H_2O)_6^{2+}$, $Ni(H_2O)_5^{2+}$, $NiBr(H_2O)_3^+$, $NiBr_2(H_2O)_{2(aq)}$	Wallen et al. (1998)
XAS, NIR and MD	25–525 °C, 1–720 bar, 0.4 m ≤ mBr ≤ 1.2 m	$Ni(H_2O)_6^{2+}$, $NiBr(H_2O)_3^+$, $NiBr_2(H_2O)_{2(aq)}$, $NiBr_3(H_2O)^-$	Hoffmann et al. (1999)
Hydroxide complexes			
Solubility	150–300 °C, P < 120 bar, 3 < pH(25 °C) < 13	$Ni(OH)^+$, $Ni(OH)_{2(aq)}$, $Ni(OH)_3^-$	Tremaine and Leblanc (1980)
Solubility	21–315 °C, 131–141 bar, 9.3 < pH(25 °C) < 11.6	$Ni(OH)^+$, $Ni(OH)_{2(aq)}$	Ziemniak and Goyette (2004)
Solubility	0–350 °C, P_{sat}, 3 < pH < 13	$Ni(OH)^+$, $Ni(OH)_{2(aq)}$	Palmer et al. (2011)

[a] Possible octahedral Ni–Cl–(H_2O) species: $Ni(H_2O)_6^{2+}$, $NiCl(H_2O)_5^+$, $NiCl_2(H_2O)_{4(aq)}$, $NiCl_3(H_2O)_3^-$, $NiCl_4(H_2O)_2^{2-}$, $NiCl_5(H_2O)^{3-}$, and $NiCl_6^{4-}$.
[b] Possible tetrahedral Ni–Cl–(H_2O) species: $NiCl(H_2O)_3^+$, $NiCl_2(H_2O)_{2(aq)}$, $NiCl_3(H_2O)^-$, and $NiCl_4^{2-}$.

Table 2
List of sample solutions: composition (all concentrations are reported on molality scale throughout this paper), temperature, pressure, and fluid density which are calculated based on NaCl concentrations from the equation of state developped by Driesner (2007) and Driesner and Heinrich (2007), and implemented in the SoWat software (http://www.geopetro.ethz.ch/people/td/sowat).

Solution	Composition [m]					Cl:Ni ratio	T (°C)	P (bar)	Density (g/cm^3)
	$Ni_{\_total}$	NaCl	LiCl	HCl	$Cl_{\_total}$				
S1	0.194	0	0	0.06	0.449	2.3	25–369	400	1.03–0.66
S2	0.198	1.063	0	0.06	1.518	7.7	25–369	400	1.07–0.73
S3	0.196	2.789	0	0.06	3.240	16.5	25–369	400	1.13–0.82
S4	0.197	4.242	0	0.06	4.696	23.8	25–369	400	1.17–0.87
S5	0.201	5.535	0	0.06	5.997	29.8	25–369	400	1.20–0.92
S6[a]	0.216	0	0	0.06	0.06	0.28	25–217	400	1.03–0.90
S7	0.296	0	0	0.03	0.626	2.1	25–434	600	1.05–0.59
S8	0.183	0	7.280	0.03	7.682	42.0	25–434	600	1.20–0.85

[a] $NiSO_4 \cdot 6H_2O_{(s)}$ was used as the source of Ni^{2+} in solution 6, and $NiCl_2 \cdot 6H_2O_{(s)}$ used in all other solutions.

solution from 0.449 m to 5.997 m. LiCl was used to achieve the highest chloride concentration (7.682 m) instead of NaCl, as the former has a higher solubility in water. The compositions and experimental conditions for the sample solutions are listed in Table 2.

2.1. Experimental setup

A custom-built high temperature and high pressure spectroscopic cell, mAESTRO (Australian Extreme SpecTROscopy), was used for the XAS measurements (Tian et al., 2010). The system (Fig. 1) is composed of a pressure generation and regulation unit, a temperature control unit, a controlling PC, and a spectroscopic autoclave based on the design of Testemale et al. (2005). The sample solution is contained within a glassy carbon tube (Sigradur G grade, HTW®) that has a length of 85 mm, an internal diameter of 4 mm and a wall thickness of 1 mm. The sample solution is sealed by the two alumina pistons with Viton O-rings. This sample tube is placed within a resistive furnace; the nichrome wire of the heater was coiled away from the beam path, and blank XAS measurements showed no Ni contamination from the heater. The tube and resistive furnace are placed in a water-cooled stainless steel autoclave, which was pressurized using He. Pressure was regulated by a PID-controlled high precision regulation unit (Bruyère et al., 2008). Three Be windows are mounted in the autoclave: one entrance window for incident X-rays, one exit window for transmitted X-rays (axial), and one exit window for fluorescence signals (at 90° relative to the X-ray beam). Beryllium windows with a thickness of 0.7 mm and 1 mm were used, allowing for data collection at 400 bar and 600 bar, respectively; only the transmission signal was measured. The experimental setup allows the temperature and pressure of the sample to be adjusted independently and maintained within ±1 bar and ±1 °C of the set values for the long periods required for the collection of EXAFS data (~40 min per scan, up to 4 scans per measurement).

2.2. XAS measurements

All XAS measurements were carried out at the XAS beamline of the Australian Synchrotron (AS), which is a 3 GeV ring synchrotron facility. This XAS beamline has a 1.9 T wiggler source and a Si (111) double-crystal monochromator with an energy resolution of 1.5×10^{-4} (ΔE/E), resulting in an energy resolution of 1.25 eV at the Ni *K*-edge (8333 eV). The beam was focused vertically using a mirror, and then horizontal and vertical slits were used to achieve the desired size. The beam spot size used was about 140 × 400 μm^2 (height × width) for the 400 bar experiments and 300 × 700 μm^2 for the 600 bar experiments. The flux was ~$6 \cdot 10^{11}$ photons/s with the larger beam size. Data were acquired in transmission mode for all XAS measurements, using 30 cm ion chambers flowing He in I_0, and N_2 in I_1 and I_2. A Ni foil was used to calibrate the beam energy.

The XAS data collected from the empty cell showed step heights of 0.0246 (0.7 mm windows) and 0.0248 (1 mm windows) at around 8340 eV due to Ni impurities in the Be windows; these step heights correspond to 338 ppm and 238 ppm Ni in the 0.7 mm and 1.0 mm windows, respectively. These Ni contaminations are comparable to ~200 ppm for Be PF-60 according to the manufacturer (Brush Wellman), and are equivalent to a concentration of ~3.72 and 3.75 mmolal Ni in the water sample for the 0.7 mm and 1 mm Be windows, respectively. This level of Ni contamination is negligible compared with the much higher concentration of Ni in the sample solution (~200 mmolal). Temperature calibration was achieved in the same manner as previous studies (*e.g.*, Etschmann et al., 2010; Liu et al., 2011) by measuring the density of water, and comparing the measurements with the water densities tabulated in the NIST database (Lemmon et al., 2000).

Sample solutions were loaded at ambient conditions. For each solution, steps were taken to achieve isobaric heating, which included: i) the mAESTRO autoclave was pressurized to the target pressure at a rate of 15 bar per minute until it remained at a constant level (400/600 bar); ii) the sample solution was heated to the target temperature at a rate of 10 °C per minute; and iii) at the set temperature and pressure, Ni *K*-edge XAS data were measured from 8133 eV to 8333 eV with an energy step of 10 eV, from 8333 eV to 8383 eV with an energy step of 0.2 eV, and onwards with a step of 0.035 in k-space to k = 13 Å^{-1}, corresponding to 8977 eV. This maximum energy is just before the Cu *K*-edge, which is visible in the spectra due to the presence of ~100 ppm Cu in the Be windows according to the manufacturer (Brush Wellman).

3. Results and data analysis

A series of XAS measurements was conducted for the solutions listed in Table 2. In this section, we first describe the results of the XANES measurements of solids and solutions, followed by a description and analysis of the EXAFS data of representative solutions. Finally, we present the results of *ab initio* simulations of the XANES spectra, based in part on optimization of the geometry of the Ni(II) chlorocomplexes *via* Density Functional Theory (DFT) calculations.

3.1. Results of XANES spectroscopy

3.1.1. XANES for Ni solid compounds

Data were collected for ten solid standards (Fig. 2) to provide qualitative 'fingerprinting' information regarding the local coordination environment (coordination geometry, number and identity of neighboring atoms) of Ni. Furthermore, these standards where the local environment of Ni is known are useful for testing the capability of *ab initio* XANES simulations to reproduce the observed features.

Nickel is six-coordinated in five of the model compounds: Ni sulfate hexahydrate — $NiSO_4 \cdot 6H_2O$ ($[Ni(H_2O)_6]$ moieties; Rousseau et al., 2000), Ni chloride hexahydrate — $NiCl_2 \cdot 6H_2O$ ($[NiCl_2(H_2O)_4]$; Kleinberg, 1969), gaspeite — $NiCO_3$ ($[NiO_6]$; Pertlik, 1986), Ni oxide — NiO ($[NiO_6]$; Sasaki et al., 1979) and vaesite — NiS_2 ($[NiS_6]$; Krill and Amamou, 1980). The XANES spectra of Ni sulfate hexahydrate and Ni chloride hexahydrate

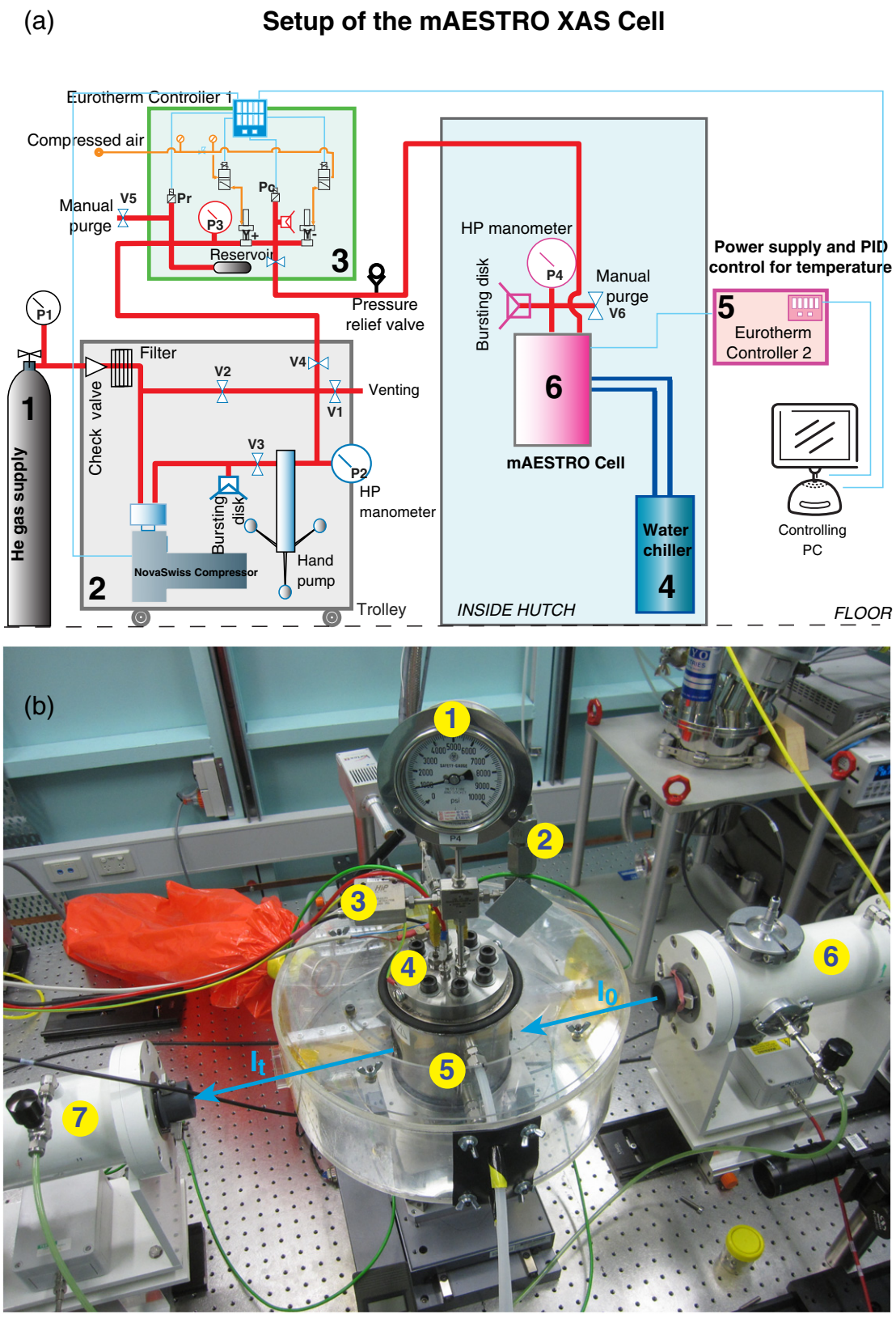

Fig. 1. mAESTRO system for *in-situ* spectroscopy on solutions under hydrothermal conditions at the Australian Synchrotron. (a) Schematic of the mAESTRO system: (1) helium supply; (2) pressure generation unit; (3) pressure regulation unit; (4) water chiller; (5) temperature control unit; (6) mAESTRO autoclave. (b) mAESTRO autoclave at the XAS beamline, Australian Synchrotron: (I_0) incident X-ray; (I_t) transmitted X-ray; (1) calibrated manometer; (2) rupture disk; (3) purge valve; (4) internal services: 2 x thermocouple ports, power inlet, pressure medium inlet; (5) cooling water inlet and outlet; (6) and (7) ionization chamber measuring I_0 and I_1, respectively.

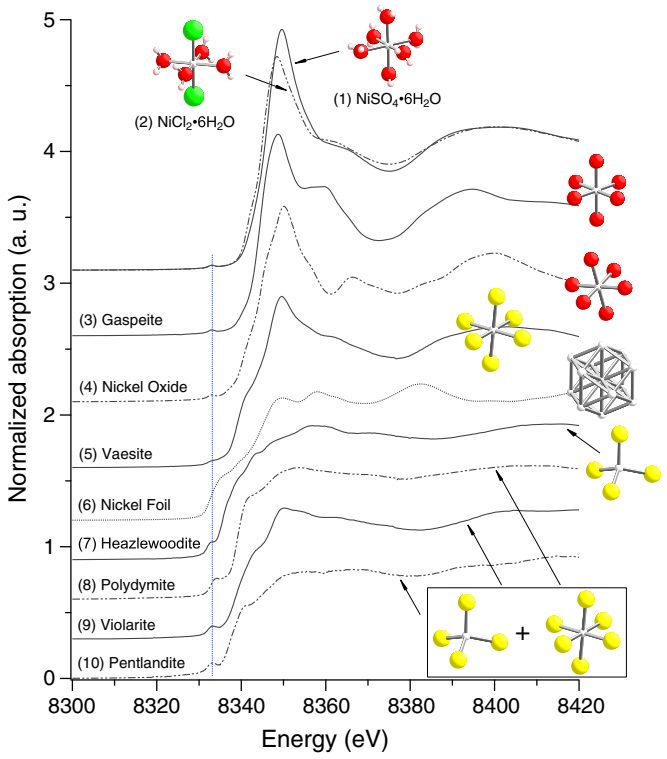

Fig. 2. Nickel *K*-edge XANES spectra for Ni model compounds. The first coordination shell of Ni for each model compounds is shown for comparison (Ni — white, Cl — green, O — red, H — pink, and S — yellow).

are very similar except for small differences in the intensity and position (1.2 eV) of the white line (feature C), as well as in the intensity of the first band (feature D) from 8360 to 8400 eV (Fig. 2). These differences can be attributed to the replacement of two water molecules by two chloride ions in $NiCl_2 \cdot 6H_2O_{(s)}$ relative to $NiSO_4 \cdot 6H_2O_{(s)}$. The general XANES spectral features of Ni compounds with 6-fold local coordination include: i) small pre-edge at around 8332 eV; ii) higher intensity of white line; and iii) significant oscillation at 8370–8420 eV (lower region of EXAFS). In contrast, the pre-edge is relatively high, and the white line is not so evident with less intensive EXAFS oscillation for the Ni compounds with full or partial 4-fold tetrahedral (T_d) local structure (100% T_d for heazlewoodite — Ni_3S_2, Parise, 1980; ~33% T_d for polydymite — Ni_3S_4, Vaughan and Craig, 1985; ~47% T_d for violarite — $Fe_{0.95}Ni_{2.05}S_4$, Tenailleau et al., 2006; and ~88% T_d for pentlandite — $Fe_{4.64}Ni_{4.36}S_8$, Tenailleau et al., 2006). These features have been used to identify the local site symmetry and electronic structure of Ni in aqueous solutions (Hoffmann et al., 1999) and in glasses and melts (Galoisy and Calas, 1993; Farges et al., 2001a,b).

3.1.2. Effect of temperature on the XANES spectra of Ni(II) chloride solutions

The Ni *K*-edge XANES spectra of solutions with various salt concentrations and Cl:Ni molar ratios are plotted in Fig. 3 as a function of temperature at constant pressures of 400 bar (S3) and 600 bar (S7–S8). Solutions S7 and S8 demonstrate the effect of temperature on the spectral evolution of the solutions containing the least and most amount of chloride: 0.626 m Cl_{tot} (S7) and 7.682 m Cl_{tot} (S8; see Table 2). The spectra of solution S3 with intermediate chlorinity (3.24 m Cl_{tot}) are also shown in Fig. 3. Details of the spectral evolution of the baseline-removed pre-edge are shown in the insets. In summary, the features of Ni *K*-edge XANES spectral evolution with increasing temperature at fixed salinity include: i) rise of the intensity of the pre-edge peak at ~8332 eV (feature A in Fig. 3); ii)

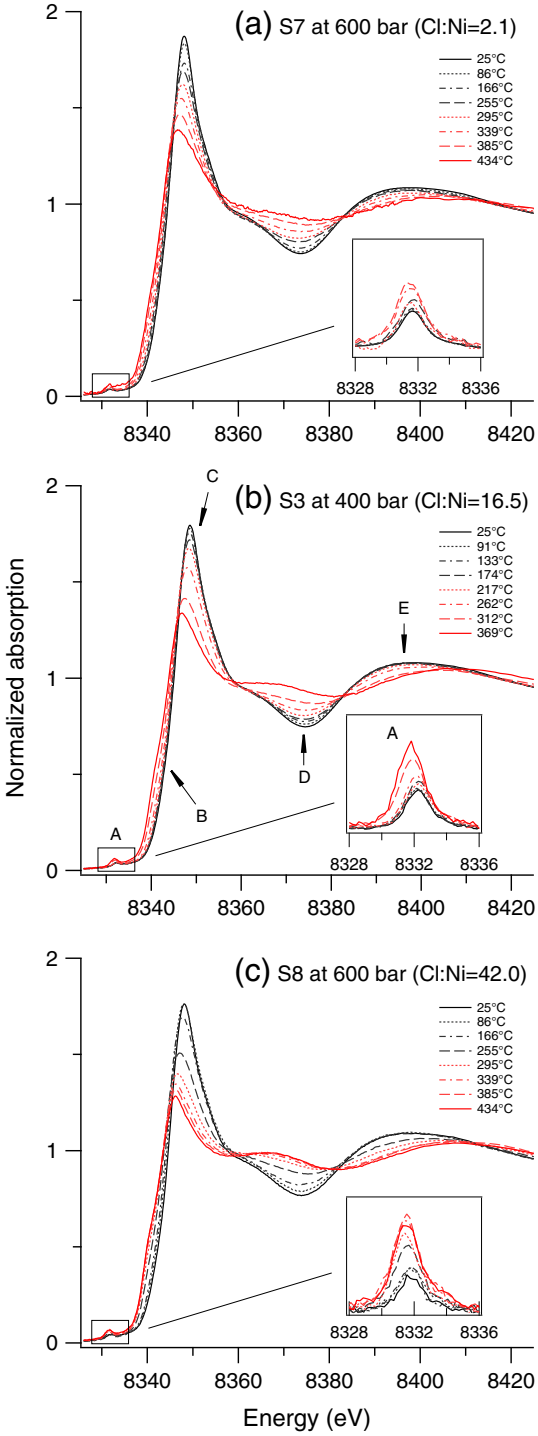

Fig. 3. Spectral evolution of nickel complexes as a function of temperature and Ni:Cl molar ratio: (a) solution S7 with Cl:Ni = 2.1 at 25–434 °C and 600 bar, (b) solution S3 with Cl:Ni = 16.5 at 25–369 °C and 400 bar, and (c) solution S8 with Cl:Ni = 42.0 at 25–434 °C and 600 bar. Baseline-removed pre-edges are shown as a function of temperature in each inset for clarity.

decrease of the white line intensity and shift of the positions of both pre-edge peak and white line towards lower energies (feature A/C in Fig. 3); iii) growth of a shoulder at ~8340 eV on the low energy side of white line (feature B in Fig. 3); and iv) reduced intensity of the oscillation in the energy range 8360 to 8420 eV (features D and E in Fig. 3). These spectral changes with increasing temperature are consistent with the trends observed in previous XAS studies of other divalent transition metals in halide solutions, such as Mn^{2+} (Chen et al., 2005b), Fe^{2+}

(Testemale et al., 2009), Co^{2+} (Liu et al., 2011), Zn^{2+} (Simonet et al., 2002; Liu et al., 2007) and Cd^{2+} (Bazarkina et al., 2010), and reflect a transition from six-coordinated (octahedral) to four-coordinated (tetrahedral-like) structures.

For all three solutions, only small changes are observed in the XANES spectra from 25 °C to 166 °C (Fig. 3), which implies that octahedral complexes are largely dominant over this temperature range. However, all the spectra begin to change significantly above 166 °C. While the spectra of the solutions S3 and S7 keep changing throughout the measured temperature range, the spectra of S8 (highest salinity solution) change rapidly from 166 °C to 339 °C, but remain nearly constant from 339 °C to 434 °C (Fig. 3). This indicates that the structural transition of Ni(II) chloride complexes in S8 occurs mainly in the temperature range 166–339 °C, with one coordination geometry predominant above 339 °C. The pre-edge is sensitive to the local geometry of the Ni site (Farges et al., 2001a,b). The pre-edge reflects a 1s→3d transition, where the electric dipole is forbidden and only weak electric quadrupole is allowed in symmetrical environments (Shulman et al., 1976; Westre et al., 1997), resulting in a small intensity of the pre-edge in octahedrally coordinated compounds (*e.g.*, $NiSO_4 \cdot 6H_2O_{(s)}$, $NiCl_2 \cdot 6H_2O_{(s)}$, $NiO_{(s)}$ and $NiCO_{3(s)}$ in Fig. 2), just like in the XANES spectra of other divalent 3d transition metal complexes at room temperature (*e.g.*, Mn(II), Chen et al., 2005a; Co(II), Liu et al., 2011; Fe(II), Testemale et al., 2009). With increasing T, the growth of pre-edge intensity is attributed to 3d–4p mixing in a non-centrosymmetric environment such as the tetrahedral geometry in this case, where electric dipole plays an important role (Shulman et al., 1976; Westre et al., 1997; Yamamoto, 2008; de Groot et al., 2009). For the XANES spectra collected at high temperature, the shoulder at 8340 eV on the lower energy side of the white line (feature B in Fig. 3) indicates the interaction between metal and halide ligands due to the 1s→4p electronic transition (Hoffmann et al., 1999), similar to Ca (Fulton et al., 2003), Fe(II) (Testemale et al., 2009) or Co(II) (Liu et al., 2011) in chloride solutions, or Mn(II) in bromide solutions (Chen et al., 2005a).

3.1.3. *Effect of chloride concentration on the XANES spectra of Ni(II) chloride solutions*

Ni *K*-edge XANES spectra are shown in Fig. 4 as a function of salinity at fixed temperatures. At 25 °C (Fig. 4a) the spectra of solutions with varying chloride concentrations are very close to those of the chloride-poor solution (S6; 0.216 m $NiSO_4$ with 0.06 m HCl). The XANES spectra of S1, S2 and S6 overlap, and the XANES spectra of the other solutions (S3, S4 and S5) show a slight decrease of white line intensity and a subtle energy shift (0.3 eV) of the white line peak to lower energy when the NaCl concentration increased from 1 to 5.5 m. This spectral evolution as a function of salinity is analogous with the difference of the XANES spectra of the solid standards ($NiSO_4 \cdot 6H_2O_{(s)}$ and $NiCl_2 \cdot 6H_2O_{(s)}$, Fig. 1), and is consistent with the progressive replacement of H_2O by Cl^- around Ni^{2+} within the first octahedral shell. Ni^{2+} is surrounded by six water molecules in the first shell of $NiSO_4 \cdot 6H_2O_{(s)}$, and aqueous Ni^{2+} exists as an octahedral $Ni(H_2O)_6^{2+}$ complex under ambient and chloride-poor conditions (Hoffmann et al., 1999). The strong similarity of the XANES spectra of $NiSO_4 \cdot 6H_2O_{(s)}$ and Cl-poor solutions (S1, S2 and S6) is consistent with the absence of an

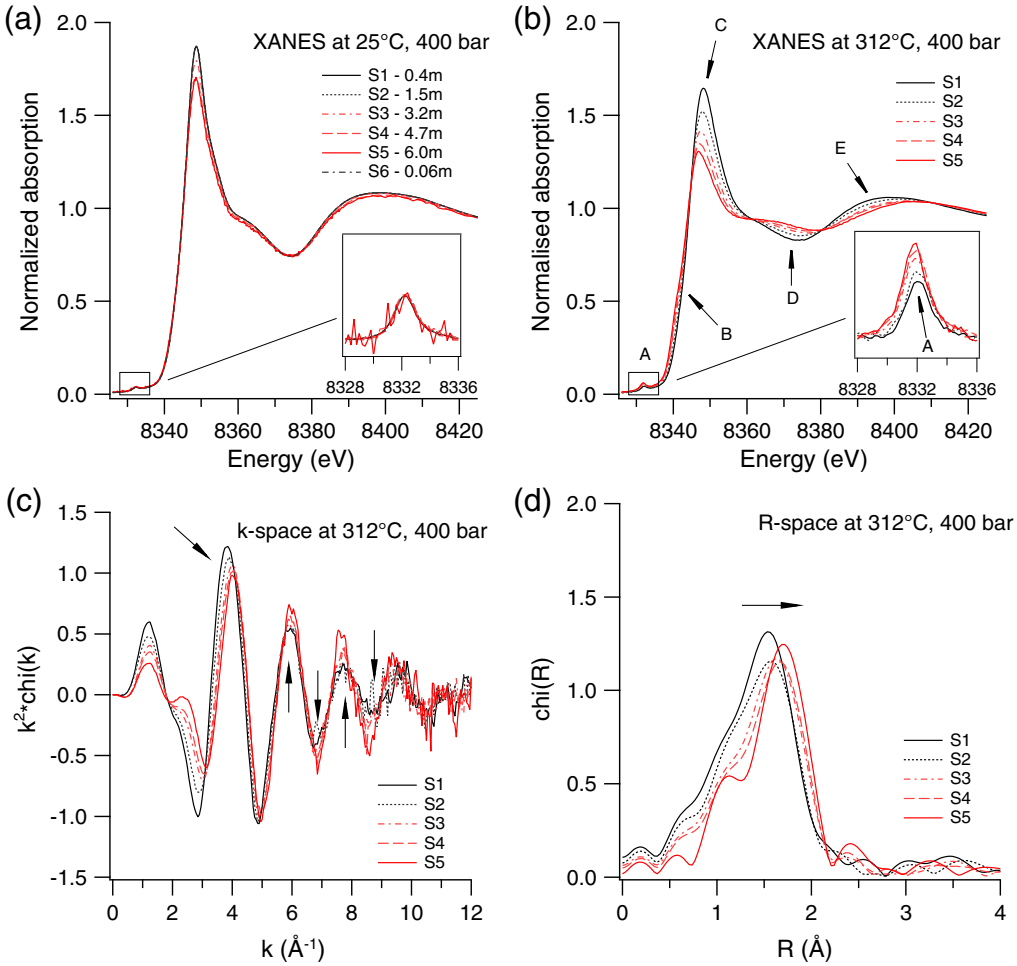

Fig. 4. Spectral evolution of nickel complexes (400 bar) as a function of salinity: (a) XANES at 25 °C for S1–S6, (b) XANES at 312 °C for S1–S5, (c) EXAFS k-space spectra at 312 °C for S1–S5, (d) Fourier transformed EXAFS R-space spectra at 312 °C for S1–S5. Baseline-removed pre-edges are shown as insets in (a) and (b) for clarity.

energy shift in the 350–550 nm absorbance band for solutions at 26 °C with increasing salinity from 0 to 1 m (Liu et al., 2012b), and suggests that there is no significant replacement of H_2O molecules by Cl^- at room temperature in low salinity solutions (m Cl<1 m).

More significant spectral changes were observed at elevated temperatures when NaCl concentrations increased from 0 to 5.5 m. For example, at 312 °C (400 bar), addition of NaCl resulted in systematic changes of XANES spectra along the direction of arrows for features A to E (Fig. 4b). The effect of increasing salinity on the XANES spectra is very similar to that of increasing temperature, and increasing temperature and salinity both favor the structural transition of Ni(II) chloride aqueous complexes from six-coordinated octahedral to four-coordinated tetrahedral-like structures. This is also reflected by the isosbestic points at around 8359 and 8382 eV in the Ni XANES spectra as a function of both temperatures and salinities (Figs. 3 and 4b). In addition, we note that there are some spectral differences between the solutions with lowest (S7) and highest (S8) Cl:Ni ratios at 434 °C in terms of the white line intensity and the shape of the band D (Fig. 3). In particular, the bump at 8370 eV was significant for S8 but absent for S7. This suggests that different tetrahedral species may exist at low and high Cl:Ni ratios.

3.2. EXAFS analysis

The changes in XANES spectra correlate with changes in EXAFS. For example, at 312 °C (400 bar) the added NaCl resulted in systematic changes for the EXAFS k-space and R-space spectra as indicated by the arrows in Fig. 4c,d. R-space spectra reflect the radial distribution function around the central Ni^{2+} atoms, and the position of the main peak moves to larger R with increasing chlorinity, which indicates an increase of bond length to neighboring ligands. In this section we describe the fitting of the EXAFS data. We first present results obtained on solutions that contain 'end-member' Ni(II) chlorocomplex structures, *i.e.* solutions in which one complex geometry is likely to dominate speciation. We use these solutions to investigate the sensitivity of the refined structural parameters to some of the fitting parameters. Then, we present fits of series of solutions in which different complex geometries may coexist, as a function of temperature and salinity.

3.2.1. EXAFS fitting of solutions where one Ni(II) complex geometry predominates

In this section we describe the fitting of the EXAFS data of the solutions in which Ni(II) is likely to exist mainly in a single coordination geometry (either octahedral or tetrahedral-like). The XANES analysis in the previous section showed that at room-T and with (almost) no salt present, the octahedral hexaaquo complex dominates Ni(II) speciation in solution S6 (Table 2). Solutions S1–S8 at 25 °C all contain octahedral complexes, and their EXAFS spectra are also fitted in this section. In contrast, at the highest T and in the saltiest solution (S8, 7.682 m Cl, 434 °C, 600 bar), the XANES spectra suggest that a tetrahedral-like complex dominates Ni speciation; the very small change in the spectrum upon heating from 339 °C to 434 °C suggests that speciation changes little in this solution, therefore this solution may be dominated by a single tetrahedral Ni(II) chlorocomplex.

Nickel EXAFS transmission data were analyzed by the HORAE software package developed by Ravel and Newville (2005). The following fitting routine was used: i) background removal and normalization of raw transmission data (Autobk program as implemented in HORAE); ii) extraction of EXAFS oscillations; and iii) EXAFS fitting of structural parameters with all calculations based on FEFF8 (Ankudinov et al., 1998). The fitted parameters include: the energy shift (ΔE_0), which is used to correct the discrepancy between E_0 and theoretical calculation; the number of oxygen (water molecule; N_O) and chlorine (N_{Cl}) in the first coordination shell of Ni^{2+}; the bond distance (R_O, R_{Cl}) from the central Ni^{2+} cation to the neighboring ligands; and the Debye–Waller factor (σ^2_O, σ^2_{Cl}) that accounts for mean-square relative displacement (*i.e.*, thermal and structural disorder) for oxygen and chlorine scattering shell. In cases where complexes with two different geometries (*i.e.*, octahedral and tetrahedral-like) exist, different stoichiometries (N), distances (R) and Debye–Waller factors (σ^2) can ideally be fitted for each geometry. A value of 0.83(07) for the amplitude factor (S_0^2) was determined by the EXAFS refinement on the data for $NiSO_4 \cdot 6H_2O_{(s)}$, which contains $[Ni(H_2O)_6]^{2+}$ moieties in the first shell (Rousseau et al., 2000). This value is close to that of 0.85 used in Hoffman et al. (1999) $NiBr_2$ XAS study, and it was fixed in all subsequent EXAFS refinements. EXAFS refinements were performed using a Hanning window. We tested the effect of refinement being performed in either k- or R-space, and of the choice of k-weighting (fitting with k^2 or multiple weighting), and found that the choice of fitting strategy had little influence on the values of the fitted parameters (*i.e.*, refined parameters were within error). We report the refined EXAFS parameters based on the k^2-weighted fits in R-space (Table 3). The goodness of fit was evaluated by two parameters: the R-factor, which is defined as a fraction of the sum of the squares of the differences between data and fit to the sum of the squares of the data; and the reduced chi-square χ^2 (see Kelly et al., 2008), which allows to compare fits with different numbers of parameters and different data qualities.

The EXAFS fit of S6 at 25 °C and 400 bar confirms a pure octahedral $Ni(H_2O)_6^{2+}$ complex ($N_O = 5.9(0.2)$) in chloride-poor solution (acidified using 0.06 m HCl). The similarity of the EXAFS data between S6 (Cl:Ni = 0.3) and S7 (Cl:Ni = 2.1) at 25 °C reveals that very limited substitution of H_2O by Cl^- takes place around Ni(II) at room temperature in solutions with low chloride concentration. Thus, $Ni(H_2O)_6^{2+}$ is likely to be the predominant Ni species in S7 at 25 °C, and the refined number of oxygen (water) around Ni^{2+} in S7 was 6.0(0.2). Attempts to add one chlorine into the first shell resulted in a statistically worse fit (*i.e.* the statistically significant difference of reduced χ^2 for the two fits is greater than two standard deviations, see equation 19 on page 445 in Kelly et al., 2008). The refined Ni – O bond distances (2.051(0.004) Å in S6, 2.050(0.004) in S7) are in excellent agreement with the literature values of 2.06(2) Å (Jong et al., 1996 and references therein), 2.052(0.007) Å (Hoffmann et al., 1999) and 2.051(0.006) Å (Merkling et al., 2002) for the Ni(II) hexaaquo complex. The refined Debye–Waller factor (σ^2) of $5.7(0.6) \times 10^{-3}$ Å^2 is also consistent with previous studies, *e.g.*, $5.9(0.7) \times 10^{-3}$ Å^2 by Wallen et al. (1998), $6.1(0.4) \times 10^{-3}$ Å^2 by Merkling et al. (2002) and $6.0(1.0) \times 10^{-3}$ Å^2 by Hoffmann et al. (1999). While the XANES spectrum of S8 at 25 °C was a typical octahedral-like spectrum, very similar to that of S6 (25 °C), the EXAFS refinement for this spectrum was conducted with the sum of O and Cl fixed to 6 and the best fit model of $NiCl_{0.9(0.6)}O_{5.1(0.6)}$ was obtained. We also tested the effect of the absence of coordination number constraint, finding that the best fit model was $NiCl_{1.3(1.3)}O_{5.2(0.6)}$. The ligand numbers of both fits were well within error, indicating that solution S8 at 25 °C contains a significant amount of low order octahedral chlorocomplexes such as $[NiCl(H_2O)_5]^+$. Correspondingly, the coordination number constraint of 6 was also applied to the EXAFS refinements for S4 and S5 at 25 °C. EXAFS reveals the presence of chloride within the octahedral complex at total chloride concentrations ≥4.7 m at room temperature (Table 3).

For refinement of the solution with high Cl:Ni ratios (S8; Cl:Ni = 42) at 434 °C and 600 bar, the coordination number of Ni was constrained to be four because the XANES analysis for this solution suggests a tetrahedral geometry (Section 3.1). As in tetrahedral coordination the Ni – Cl and Ni – O distances are relatively close, and distinguishing O from Cl is challenging due to their similar scattering, unrealistic numbers of O and Cl (more than 12) were obtained with the absence of coordination number constraint. With coordination number constrained to 4, the refined number of chlorine around Ni was 2.6(1.0) (Table 3), which is smaller than the number of four for fully chlorinated metal complexes, *e.g.*, $FeCl_4^{2-}$ (Testemale et al., 2009), $CoCl_4^{2-}$ (Liu et al., 2011), and $ZnCl_4^{2-}$ (Mayanovic et al., 1999). The absence of a fully chlorinated tetrahedral species, but instead the presence of at least one coordinated water molecule even at high salinity and high temperature, is consistent

Table 3
Refined EXAFS parameters for selected solutions at extreme temperatures and chlorinities.

Sample−T (°C)	ΔE_0(eV)	Ni–O interaction			Ni–Cl interaction			k-range	R-range	R-factor	χ^2
		N_O	R_{Ni-O}(Å)	σ^2_O(Å$^2\times10^{-3}$)	N_{Cl}	R_{Ni-Cl}(Å)	σ^2_{Cl}(Å$^2\times10^{-3}$)				
S1−25	−2.8(0.4)	5.9(0.2)	2.050(04)	5.6(0.6)	–	–	–	2−−11	1–4.1	0.005	277.34
S2−25	−3.0(0.4)	5.9(0.2)	2.050(04)	5.8(0.6)	–	–	–	2–11	1–4.1	0.005	228.72
S3−25	−2.9(0.4)	5.8(0.2)	2.052(04)	5.7(0.6)	–	–	–	2–11	1–4.1	0.005	143.46
S4−25	−2.3(0.6)	[a]5.3(0.4)	2.049(06)	4.8(0.8)	[a]0.7(0.4)	2.441(81)	26.5(12.6)	2–11	1–4.3	0.007	45.97
S5−25	−2.6(0.7)	[a]5.1(0.5)	2.046(08)	5.0(1.0)	[a]0.9(0.5)	2.370(54)	24.6(10.2)	2–10	1–4.3	0.006	7.66
S6−25	−3.0(0.4)	5.9(0.2)	2.051(04)	5.7(0.6)	–	–	–	2–11	1–4.1	0.005	331.31
S7−25	−2.7(0.4)	6.0(0.2)	2.050(04)	5.7(0.6)	–	–	–	2–11	1–4.1	0.005	235.07
S8−25	−3.6(1.0)	[a]5.1(0.6)	2.040(11)	6.1(1.0)	[a]0.9(0.6)	2.321(26)	9.8(5.0)	2–11	1–4.3	0.009	21.95
S8−25	−3.8(1.3)	5.2(0.6)	2.042(13)	6.6(1.3)	1.3(1.3)	2.309(42)	15.8(12.7)	2–11	1–4.3	0.009	22.98
S8−434	1.5(4.6)	[a]1.4(1.0)	2.100(21)	[b]6	[a]2.6(1.0)	2.284(29)	[b]10	2–10	1–3	0.017	22.60
[c]S7−385	−3.6(0.8)	[b]2.78	[b]2.04 (oct)	11.1(4.0)	[b]1.82	–	–	2–10	1–3	0.038	98.87
[b]frac = 0.7			[b]2.10 (tet)	11.1(4.0)		2.276(14) (tet)	12.3(2.4)				
[d]S7−385	−1.8(1.5)	2.8(1.2)	[b]2.04 (oct)	8.9(4.1)	1.6(1.0)	–	–	2–10	1–3	0.031	90.70
frac = 0.80(10)			[b]2.10 (tet)	8.9(4.1)		[b]2.27 (tet)	12.6(4.3)				
[e]S7−385	−1.8(1.4)	2.8(1.2)	[b]2.04 (oct)	9.0(4.4)	1.7(1.0)	[b]2.32 (oct)	12.8(4.4)	2–10	1–3	0.030	90.36
frac = 0.79(11)			[b]2.10 (tet)	9.0(4.4)		[b]2.27 (tet)	12.8(4.4)				
[f]S7−385	−1.7(1.4)	2.7(1.2)	[b]2.04 (oct)	9.0(4.6)	1.8(0.9)	[b]2.32 (oct)	13.1(4.4)	2–10	1–3	0.031	91.34
frac = 0.77(12)			[b]2.10 (tet)	9.0(4.6)		[b]2.27 (tet)	13.1(4.4)				
[g]S7−385	−1.7(1.3)	2.6(1.1)	[b]2.04 (oct)	8.7(4.6)	1.9(0.9)	[b]2.32 (oct)	13.6(4.3)	2–10	1–3	0.032	93.99
frac = 0.76(12)			[b]2.10 (tet)	8.7(4.6)		[b]2.27 (tet)	13.6(4.3)				

[a] Sum of number of O and Cl fixed to be equal to 6 (25 °C) or 4 (434 °C).
[b] Value fixed (not optimized) during refinements.
[c] Fitted by a linear combination of 70%(fixed) $NiCl_{2.6}O_{1.4}$ and 30%(fixed) NiO_6.
[d] Fitted by a linear combination of 80(±10)% $NiCl_{2.0}O_{2.0}$ and 20(±10)% NiO_6.
[e] Fitted by a linear combination of 79(±11)% $NiCl_{2.0}O_{2.0}$ and 21(±11)% $NiCl_{0.5}O_{5.5}$.
[f] Fitted by a linear combination of 77(±12)% $NiCl_{2.0}O_{2.0}$ and 23(±12)% $NiCl_{1.0}O_{5.0}$.
[g] Fitted by a linear combination of 76(±12)% $NiCl_{2.0}O_{2.0}$ and 24(±12)% $NiCl_{1.5}O_{4.5}$.

with the $NiBr_{3.3(0.6)}O_{1.0(0.2)}$ average ligation at 425 °C, 410 bar with Br:Ni ratio of ~6 (Hoffmann et al., 1999) and the $CdCl_{3.4(0.6)}O_{1.0(0.6)}$ model at 450 °C, 600 bar with Cl:Cd ratio of ~238 (Bazarkina et al., 2010).

3.2.2. Solutions containing a mixture of octahedral and tetrahedral complexes

Fitting of the EXAFS data of solutions that contain a mixture of octahedral and tetrahedral-like complexes is challenging, because each geometry has different Ni−O and Ni−Cl distances, Cl/O ratio, and Debye–Waller factors. Single solution EXAFS data do not provide enough information for fitting such mixtures; in order to retrieve the correct answer, information from several solutions must be combined, ideally together with information from XANES data. We checked a number of models and methods, and report results based on the assumption that solutions that contain mixtures of octahedral and tetrahedral-like complexes can be modeled as linear combinations of solutions in which a single complex geometry was dominant. The aim was to fit the intermediate spectra using the minimum number of parameters.

At 434 °C, the XANES data show that speciation is dominated by tetrahedral-like complexes, and suggest that significant differences exist in the speciation at high and low Cl:Ni ratios. Unfortunately, the EXAFS data for S7 (Cl:Ni = 2.1) at 434 °C was too noisy to be analyzed. The spectrum for S7 at 385 °C shows both octahedral and tetrahedral-like spectral features, which suggests that both octahedral and tetrahedral species are present as a mixture. We modeled the XANES spectrum of S7 at 385 °C as a linear combination of 30% NiO_6 (solution S7 at 25 °C) and 70% $NiCl_{2.6}O_{1.4}$ (solution S8 at 434 °C); this indicates that S7 consists of about 70% of tetrahedral complex at 385 °C. The EXAFS data of S7 at 385 °C was modeled as a mixture of these octahedral and tetrahedral-like components, following this procedure: i) fix the fraction of the two end-members to be that determined from the XANES linear combination fit; ii) constrain the bond lengths to be within the error range of those determined from the octahedral and tetrahedral end-members; and iii) refine ΔE_0 and the Debye–Waller factors of Cl and O (the Debye–Waller factors for the oxygen and chloride atoms represent the average of the Debye–Waller factors of these atoms in octahedral and tetrahedral-like coordination). In addition, we also fitted the S7 data at 385 °C by changing the end-member model $NiCl_{2.6}O_{1.4}$ to be $NiCl_2O_2$ to reflect the mass balance constraints of the solution (Cl:Ni ~ 2) and obtained a series of good fits by varying the number of chlorine in the octahedral model (from 0 to 1.5) and refining the fraction of octahedral and tetrahedral models (Table 3). The differences of EXAFS refinements between these octahedral models as a function of octahedral chloride number from 0 to 1.5 are quite small (see R-factors and χ^2 in Table 3); the best fit was found based on a linear combination of $NiCl_{0.5}O_{5.5}$ and $NiCl_2O_2$, resulting in the average stoichiometry of $NiCl_{1.7(1.0)}O_{2.8(1.2)}$. The $NiCl_{1.82}O_{2.78}$ composition obtained using the simplest model (linear combination of 30% NiO_6 and 70% $NiCl_{2.6}O_{1.4}$) is within error of this average composition, and we used the $NiCl_{1.82}O_{2.78}$ composition for subsequent analysis due to its simplicity and agreement with the best fit. Solutions S1 to S5 at 369 °C were fitted in a similar manner (five datasets for S1, S2, S3, S4, and S5; see Table 5), using the parameters for the 'end-member' solutions shown in Table 3, and the fractions of 'end-members' determined by XANES linear combination fits from Table 4. Fig. 5 shows the experimental and fitted EXAFS spectra for solutions S7 and S8 at two extreme temperatures and for solutions S1 to S5 at 25 and 369 °C.

We also fitted the EXAFS data for solutions S8 and S7 as a function of temperature, in order to obtain a view of the change in ligation in these solutions with high and low Cl:Ni ratios as a function of temperature. The EXAFS data for S8 (seven datasets at 86, 166, 212, 255, 339 and 385 °C) were fitted simultaneously as a linear combination of S8 (25 °C) and S8 (434 °C). The same method was used for S7 (five datasets at 86, 166, 255, 295 and 339 °C) as a linear combination of S7 (25 °C) and S7 (385 °C). Refined structural parameters are listed in Table 5, and the numbers of oxygen (water molecules) and chlorine around Ni^{2+} are shown in Fig. 6 as a function of salinity and temperature. At room temperature a transition from $[Ni(H_2O)_6]^{2+}$ to $[NiCl(H_2O)_5]^{+}$ is observed (Table 3; Fig. 6a). At 369 °C, the tetrahedral complexes dominate, and again a slight increase in the number of chloride ions bonded to Ni is observed with increasing salt concentration (Fig. 6b). Fig. 6c,d illustrates the octahedral to 4-fold coordination change upon heating, together with the increasing affinity Ni(II)

Table 4
Linear combination fitting of XANES spectra for S7 and S8 at intermediate temperatures and S1 to S5 at 369 °C.

Sample — T (°C)	Fraction S7 25 °C	Fraction S7 385 °C
S7 — 25	1.0	0
S7 — 86	0.953(3)	0.047(3)
S7 — 166	0.764(8)	0.236(8)
S7 — 255	0.635(7)	0.365(7)
S7 — 295	0.471(8)	0.529(8)
S7 — 339	0.237(6)	0.763(6)
S7 — 385	0	1.0
Sample — T (°C)	Fraction S8 25 °C	Fraction S8 434 °C
S8 — 25	1.0	0
S8 — 86	0.967(4)	0.033(4)
S8 — 166	0.912(9)	0.088(9)
S8 — 212	0.793(9)	0.207(9)
S8 — 255	0.542(7)	0.458(7)
S8 — 295	0.292(5)	0.708(5)
S8 — 339	0.139(3)	0.861(3)
S8 — 385	0.064(1)	0.936(1)
S8 — 434	0	1.0
Sample — T (°C)	Fraction S1 25 °C	Fraction S7 385 °C
S1 — 369	0.28(2)	0.72(2)
Sample — T (°C)	Fraction S(2–5) 25 °C	Fraction S8 434 °C
S2 — 369	0.213(3)	0.787(3)
S3 — 369	0.152(4)	0.848(4)
S4 — 369	0.047(1)	0.953(1)
S5 — 369	0.056(7)	0.944(7)

for chloride with increasing temperature, which reflects the higher affinity for chloride of 4-fold relative to 6-fold complexes.

3.3. Density Functional Theory calculations

Density Functional Theory (DFT) calculations on Ni–Cl–H_2O clusters were performed with the Amsterdam Density Functional program, ADF2010.02 (te Velde et al., 2001) to optimize the geometries and predict bond lengths of the proposed Ni–Cl complexes. ADF implements Density Functional Theory for finite clusters and molecules using the linear combination of atomic orbital formalism. In the ADF code, the basic functions are localized Slater-type orbitals. For all atoms, an uncontracted, triple-zeta basis set (TZP) was used with polarization functions. The core orbitals of Ni (1s, 2s), Cl (1s, 2s) and O (1s) were frozen during the calculation. The parameterization of VWN (Vosko et al., 1980) was used for Local Density Approximation (LDA), together with the Perdew–Burke–Ernzerhof (PBE) (Perdew et al., 1996) generalized gradient approximation (GGA) for calculating the exchange-correlation energy (Parr and Yang, 1989). All calculations were done using the spin-unrestricted formalism to account for the two unpaired 3d-electrons of Ni. The geometry optimizations of Ni–Cl–H_2O clusters were based on a Newton–Raphson approach and the Hessian matrix as coded in ADF. The bond lengths and angles converged to 0.01 Å and 0.5°, respectively. The Conductor-like Screening model (COSMO) was employed to account for the long-range solvation field of aqueous solutions (Pye and Ziegler, 1999). In COSMO models, each atom is surrounded by a sphere of radius $R_a = 1.17 \times R_a^{vDW}$ (where R_a^{vDW} is the van der Waals radius of the atom), as optimized by Klamt and Schuurmann (1993). Here the radii of 2.1 Å for Ni, 1.72 Å for O, and 2.05 Å for Cl were used in the calculations. The radius of the solvent is 1.3 Å for H_2O and different dielectric constants (Fernandez et al. 1997) were chosen to model the aqueous phase at room temperature and at hydrothermal conditions. No significant difference in geometry was observed for calculations performed with a dielectric constant of 78 (25 °C, 1 bar) or 10 (~430 °C, 600 bar).

The optimized geometries of 6-fold and 4-fold Ni species are illustrated in Fig. 7 and the geometrical parameters are listed in Table 6. The 4-fold complexes $[NiCl_4]^{2-}$, $[NiCl_3(H_2O)]^-$ and $[NiCl_2(H_2O)_2]_{(aq)}$ all display a distorted tetrahedral structure rather than square planar geometry. The calculated Ni – Cl and Ni – O bond lengths of the tetrahedral species are shorter than those of octahedral species. Within each coordination geometry, ligand exchange reactions cause only small changes in bond lengths. The optimized Ni – O and Ni – Cl bond lengths are overall in good agreement with the values refined from the EXAFS data (Tables 3). The experimental Ni – O distance in octahedral complexes (2.050(10) Å) is close to the calculated one (2.08–2.11 Å; Table 6), and the octahedral Ni – Cl experimental distance of 2.321(26) Å is similar to the calculated distance of 2.34 Å for $[NiCl(H_2O)_5]^+$. For the tetrahedral complexes, the experimental Ni – Cl and Ni – O distances refined from solution 8 at 434 °C (Table 3) were 2.284(29) Å and 2.100(21) Å, respectively, within range of the predicted values for $[NiCl_3(H_2O)]^-$: 2.26 Å and 2.06 Å.

3.4. Ab initio XANES simulation

XANES is a sensitive probe of the local 3-D geometry around the absorbing atom. The results of the EXAFS refinements (coordination number, bond distance) and DFT-optimized geometries of aqueous Ni species were utilized to generate a number of possible geometries for the Ni(II) aqueous complexes. XANES spectra calculated *via ab initio* methods for these structures were compared to experimental spectra in order to determine the influence of structural and electronic parameters on the spectra, and to further test the speciation model derived from the quantitative EXAFS and qualitative XANES analyses.

Ab initio XANES spectra of solid standards (Fig. 8) and aqueous clusters (Fig. 9) were calculated using FDMNES (Joly, 2001) following the procedure outlined in recent metal complex studies (Brugger et al., 2007; Testemale et al., 2009; Etschmann et al., 2010; Liu et al., 2011, 2012a). All the Ni XANES simulations in this study were carried out using the finite difference method, which avoids the limitations of the muffin tin approximation by allowing a free potential shape, and is of particular interest in the case of low-symmetry and/or non-dense structures (Joly, 2001). To compare to the experimental spectra, the calculated raw spectra (photo-absorption cross-sections) were convoluted with a Lorentzian function of energy-dependent width to reproduce the core-hole lifetime broadening and the inelastic plasmon interactions with the photoelectron; the width of the function varies from 1.44 eV at the Ni *K*-edge (Ni *K* core-hole life time; Krause and Oliver, 1979) to ~15 eV at 100 eV above the edge. In addition, the spectra were convoluted with a Gaussian function (1.25 eV FWHM) to account for the energy resolution of the beamline. These convolution parameters were fixed for all calculations and not fitted in the subsequent analyses. The Fermi energy levels calculated by FDMNES were used for the convolution of the spectra of the solids, and fixed to −6 eV for the aqueous species. All calculations were carried out with neutral atoms: as the experimentally observed changes are essentially structural, we did not study the evolution of the charges on the atoms (Joly et al., 1999; Testemale et al., 2004). We evaluated the effect of introducing hydrogen atoms on the XANES calculation of the $[NiCl_3(H_2O)]^-$ cluster by comparing calculated XANES spectra of $NiCl_3(H_2O)$ and $NiCl_3O$ (Fig. 9b). These calculations show that the addition of the hydrogen atoms resulted in small changes not only in the intensity of the main bands, but also in the positions of the pre-edge (0.8 eV) and bands D and E (~2 eV) (Fig. 9b). We note that the differences are relatively small, and that hydrogen atoms are likely to be affected by significant thermal and structural disorder (*e.g.*, rotational) at high P–T conditions, so that the effect of the H-atoms on the XANES spectrum is expected to be smaller than for a static configuration (*e.g.*, Testemale et al., 2009; Liu et al., 2012a). Since the focus of this study is about deciphering the stoichiometry and geometry of the complexes (*i.e.*, first coordination shell of Ni), the effects of the H-atoms were not taken into account in the subsequent XANES calculations.

Experimental and calculated spectra of Ni solid compounds containing Ni(II) in octahedral (a–d) and tetrahedral (f) coordination

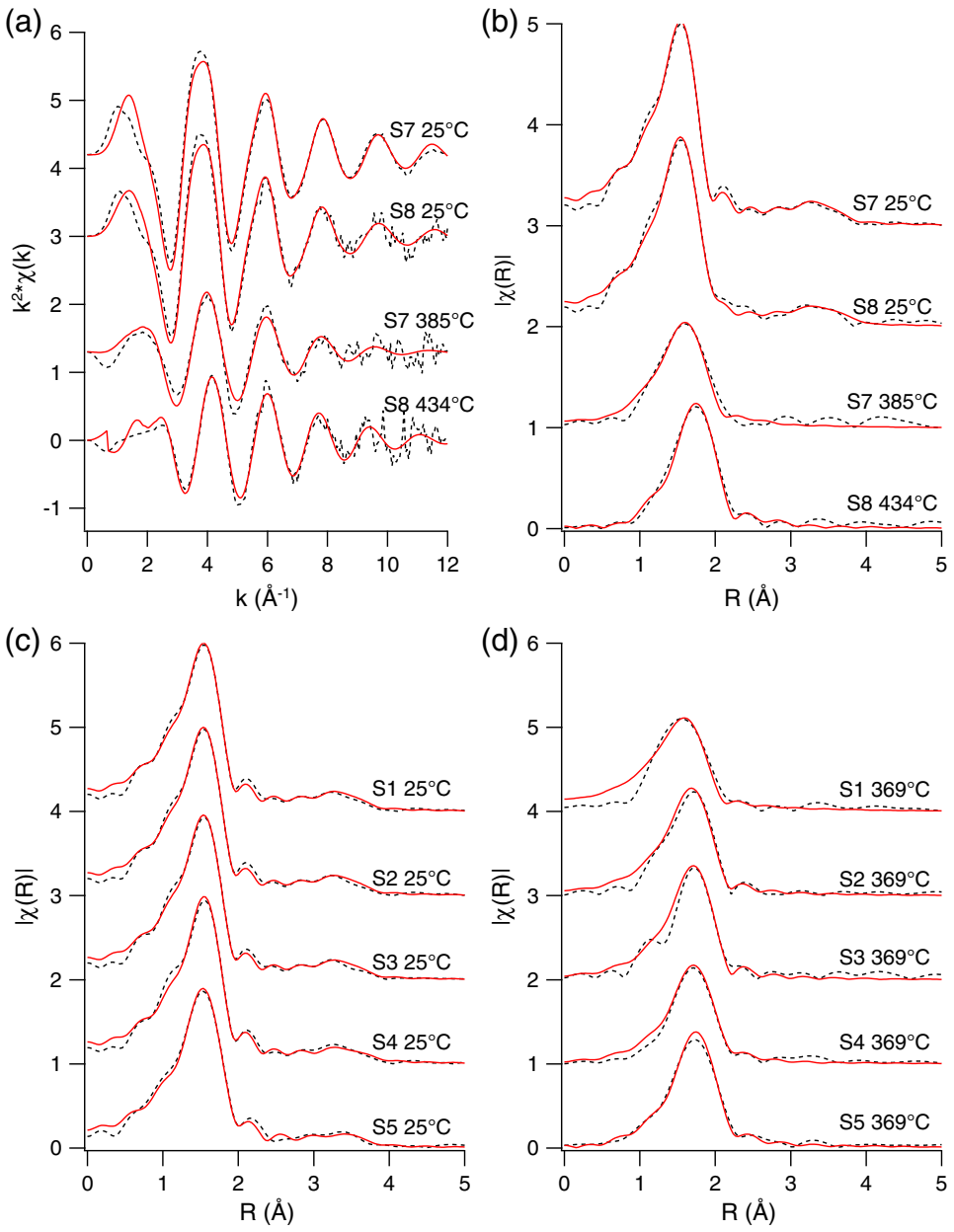

Fig. 5. Experimental (black dotted line) and fitted (red solid line) EXAFS spectra: (a) S7 at 25 °C/385 °C and S8 at 25 °C/434 °C in k-space; (b) S7 at 25 °C/385 °C and S8 at 25 °C/434 °C in R-space; (c) S1–S5 at 25 °C in R-space; (d) S1–S5 at 369 °C in R-space. All fits are shown with k^2 weighting.

are compared in Fig. 8 in order to estimate the reliability of the simulations. For all Ni compounds, calculations were carried out to radii of 3 Å (including only the nearest neighbors) and 6 Å (which takes into account contributions beyond the first shell); increasing the radius further did not produce significant changes in the calculated spectra. Overall, the calculated spectra were in good agreement with the experimental spectra, with the positions (see raw spectra) and relative intensities (convoluted spectra) of the observed band reproduced accurately. The shape of the white line (in particular a shoulder on the high energy side) and feature D is sensitive to the second shell, with large differences between the calculations conducted using 3 and 6 Å radii. The main discrepancy is the pre-edge intensity that is over-calculated compared to the experimental spectra; however, the position of the pre-edge as well as its relative intensity among different compounds are correctly reproduced.

The XANES spectra of the octahedral Ni complexes $[Ni(H_2O)_6]^{2+}$, $[NiCl(H_2O)_5]^{+}$ and $[NiCl_2(H_2O)_4]_{(aq)}$ were calculated based on the DFT optimized structures (Fig. 7) with the Ni–O distance of 2.05 Å and Ni–Cl distance of 2.34 Å (Tables 3 and 6). These values of bond lengths are within the (one sigma) error range of the EXAFS refinements and DFT calculations (±5%). The experimental spectrum for the low salinity solution S7 at 25 °C is well reproduced by the $[NiO_6]$ unit except for two small disagreements of overestimated pre-edge and underestimated white line (Fig. 9a), consistent with $[Ni(H_2O)_6]^{2+}$ being dominant at room T and low salinity. The underestimated white line is due to absence of second hydration shell as shown by D'Angelo et al. (2006). The replacement of one water molecule by a chloride ligand causes a decrease of white line intensity (feature C), an increase of the pre-edge and band D intensity, and a red shift of pre-edge position (feature A). Further chloride substitutions cause similar small spectral changes in the position and intensity of pre-edge, white line and band D. The spectral evolution of the amplitude of the white line upon chlorination is in good agreement with the evolution observed experimentally at 25 °C upon increase in salinity (Fig. 4a). No changes of the

Table 5
Refined EXAFS parameters (as a linear combination of end member spectra) for intermediate temperatures and solutions.

Sample—T (°C)	ΔE_0(eV)	Ni–O interaction			Ni–Cl interaction			k-range	R-range	R-factor/χ^2
		N_O	R_{Ni-O}(Å)	σ^2_O(Å^2)	N_{Cl}	R_{Ni-Cl}(Å)	σ^2_{Cl}(Å^2)			
S7—86	−6.0(0.2)	[a]5.85	[a]2.05 (oct)	7.0(0.5)	[a]0.09	–	–	2–10	1–4.1	0.025/455.72
			[a]2.10 (tet)	7.0(0.5)		[a]2.28 (tet)	[a]5			
S7—166	−6.3(0.4)	[a]5.24	[a]2.05 (oct)	8.1(0.9)	[a]0.43	–	–	2–10	1–4.1	
			[a]2.10 (tet)	8.1(0.9)		[a]2.28 (tet)	[a]6			
S7—255	−6.0(0.8)	[a]4.82	[a]2.05 (oct)	10.4(2.6)	[a]0.66	–	–	2–10	1–4.1	
			[a]2.10 (tet)	10.4(2.6)		[a]2.28 (tet)	5.1(6.7)			
S7–295	−5.6(1.7)	[a]4.30	[a]2.05 (oct)	11.1(6.0)	[a]0.96	–	–	2–10	1–3	
			[a]2.10 (tet)	11.1(6.0)		[a]2.28 (tet)	6.2(9.9)			
S7—339	−5.2(1.4)	[a]3.54	[a]2.05 (oct)	11.6(6.5)	[a]1.39	–	–	2–10	1–3	
			[a]2.10 (tet)	11.6(6.5)		[a]2.28 (tet)	10.0(8.6)			
S8—86	−6.6(0.5)	[a]4.98	[a]2.04 (oct)	7.4(1.3)	[a]0.96	[a]2.32 (oct)	7.2(2.8)	2–10	1–4.2	0.027/70.05
			[a]2.10 (tet)	7.4(1.3)		[a]2.28 (tet)	7.2(2.8)			
S8—166	−7.1(0.5)	[a]4.77	[a]2.04 (oct)	7.8(1.3)	[a]1.05	[a]2.32 (oct)	8.8(2.7)	2–10	1–4.2	
			[a]2.10 (tet)	7.8(1.3)		[a]2.28 (tet)	8.8(2.7)			
S8—212	−6.4(0.5)	[a]4.33	[a]2.04 (oct)	10.2(1.6)	[a]1.25	[a]2.32 (oct)	7.2(2.0)	2–10	1–4.2	
			[a]2.10 (tet)	10.2(1.6)		[a]2.28 (tet)	7.2(2.0)			
S8—255	−5.8(0.4)	[a]3.41	[a]2.04 (oct)	10.9(1.9)	[a]1.68	[a]2.32 (oct)	7.9(1.6)	2–10	1–3	
			[a]2.10 (tet)	10.9(1.9)		[a]2.28 (tet)	7.9(1.6)			
S8—295	−3.2(0.7)	[a]2.48	[a]2.04 (oct)	11.9(4.7)	[a]2.10	[a]2.32 (oct)	7.1(1.9)	2–10	1–3	
			[a]2.10 (tet)	11.9(4.7)		[a]2.28 (tet)	7.1(1.9)			
S8—339	−0.6(0.7)	[a]1.91	[a]2.04 (oct)	7.4(5.1)	[a]2.36	[a]2.32 (oct)	7.5(2.1)	2–10	1–3	
			[a]2.10 (tet)	7.4(5.1)		[a]2.28 (tet)	7.5(2.1)			
S8—385	0.4(0.8)	[a]1.64	[a]2.04 (oct)	5.3(5.7)	[a]2.49	[a]2.32 (oct)	8.9(2.6)	2–10	1–3	
			[a]2.10 (tet)	5.3(5.7)		[a]2.28 (tet)	8.9(2.6)			
S1—369	[a]−1.6	[a]3.58	[a]2.05 (oct)	14.7(4.5)	[a]1.31	–	–	2–10	1–3	0.053/159.92
			[a]2.10 (tet)	14.7(4.5)		[a]2.28 (tet)	10.1(5.5)			
S2—369	2.5(1.5)	[a]2.28	[a]2.05 (oct)	11.6(7.3)	[a]2.05	–	–	2–10	1–3	
			[a]2.10 (tet)	11.6(7.3)		[a]2.28 (tet)	[a]9			
S3—369	3.1(0.9)	[a]1.90	[a]2.05 (oct)	[a]11	[a]2.20	–	–	2–10	1–3	
			[a]2.10 (tet)	[a]11		[a]2.28 (tet)	7.8(2.0)			
S4—369	4.4(0.4)	[a]1.58	[a]2.05 (oct)	[a]6	[a]2.51	[a]2.37 (oct)	13.1(1.1)	2–10	1–3	
			[a]2.10 (tet)	[a]6		[a]2.28 (tet)	13.1(1.1)			
S5—369	8.2(1.2)	[a]1.61	[a]2.05 (oct)	[a]6	[a]2.50	[a]2.37 (oct)	10.2(3.0)	2–10	1–3	
			[a]2.10 (tet)	[a]6		[a]2.28 (tet)	10.2(3.0)			

[a] Value fixed (not optimized) during refinements.

intensity and position of the pre-edge peak were observed (inset in Fig. 4a), contrary to the prediction of the XANES simulation (Fig. 9a); this may be related to the fact that $[Ni(H_2O)_6]^{2+}$ is the major species at 25 °C from 0 to 6 m Cl with the proportion of species such as $[NiCl(H_2O)_5]^+$ and $[NiCl_2(H_2O)_4]_{(aq)}$ below 50% according to the thermodynamic analysis in the next section. Hence, the XANES calculations are consistent with the EXAFS data showing that limited ligand exchange (H_2O replaced by Cl^-) takes place progressively with increasing chloride concentration within octahedral complexes. The same observations and conclusions were made for similar experimental conditions for Fe(II) (Testemale et al., 2009) and Co(II) (Liu et al., 2011) octahedral species.

At high temperatures, qualitative analysis suggested that tetrahedral-like species dominate in solution. The effect of the complex stoichiometry on the XANES spectra was investigated by comparing the spectra calculated for a series of 4-fold complexes optimized by DFT: $[NiCl_2(H_2O)_2]_{(aq)}$, $[NiCl_3(H_2O)]^-$ and $[NiCl_4]^{2-}$ (Fig. 9c); and the effect of complex geometry by comparing different geometries for the $[NiCl_3(H_2O)]^-$ complex (Fig. 9d): square planar (D_{4h}), regular tetrahedral (T_d) and distorted tetrahedral optimized by DFT, all with the same Ni – O distance of 2.06 Å and Ni – Cl distance of 2.26 Å (Table 6). As the number of chloride increases from two to four in the cluster, the intensities of the pre-edge (feature A), white line (feature C), and bands D and E all increase, and the position of the white line shifts to lower energy (Fig. 9c). The calculations reveal that $[NiCl_4]$ provides the poorest agreement, because of the large intensity of feature D and the sharpness and energy shift of the white line. The calculated spectrum for the $[NiCl_3O]$ cluster appears to be in better agreement with the experimental spectrum (S8 at 434 °C) than those of $[NiCl_2O_2]$ and $[NiCl_4]$, in terms of shape and position of white line and feature D (Fig. 9c). The DFT optimized geometries suggest a distorted tetrahedral geometry, but many Ni(II) complexes adopt a (distorted) square planar geometry, and isomers in which Ni(II) halide complexes exist in either tetrahedral or square planar geometries are known (Hayter and Humiec, 1965). The XANES calculations in Fig. 9d reveal that the shape of the white line and feature D was well calculated for the two tetrahedral models, while the D_{4h} model produced a shifted feature D and slimmer white line. Feature B is prominent in the D_{4h} configuration, but is absent in the pure T_d geometry. This feature can be seen on the weak shoulder in raw spectrum of the optimized configuration (Fig. 9b), and finds its origin in the distortion of the tetrahedral cluster, as it was observed for the $[CoCl_4]$ moiety in a solid compound (Liu et al., 2011). The distorted T_d structure obtained *via* DFT optimization exhibits the most comprehensive agreement with the experimental data (Fig. 9d). Hence, based on the DFT geometry optimization and *ab initio* XANES calculations, a distorted tetrahedral species such as $[NiCl_3(H_2O)]^-$ is most likely the predominant species under high T and high salinity conditions. At low Cl:Ni ratio (compare 434 °C data for S7 and S8, Fig. 3a,c), the main differences among the spectra are that the intensities of the bands D and E are lower in the low salinity solution; also, the white line appears to be broader. These small differences are consistent with $[NiCl_2O_2]$ being dominant over $[NiCl_3O]$ at a Cl:Ni ratio of ~2 (Fig. 9c). Again, the same trends were observed for Fe(II) and Co(II) calculated XANES spectra (Testemale et al., 2009; Liu et al., 2011).

4. Discussion

4.1. Nickel speciation in chloride brines

The combination of qualitative XANES analysis, quantitative EXAFS refinements, DFT structure optimizations, and *ab initio* XANES simulations

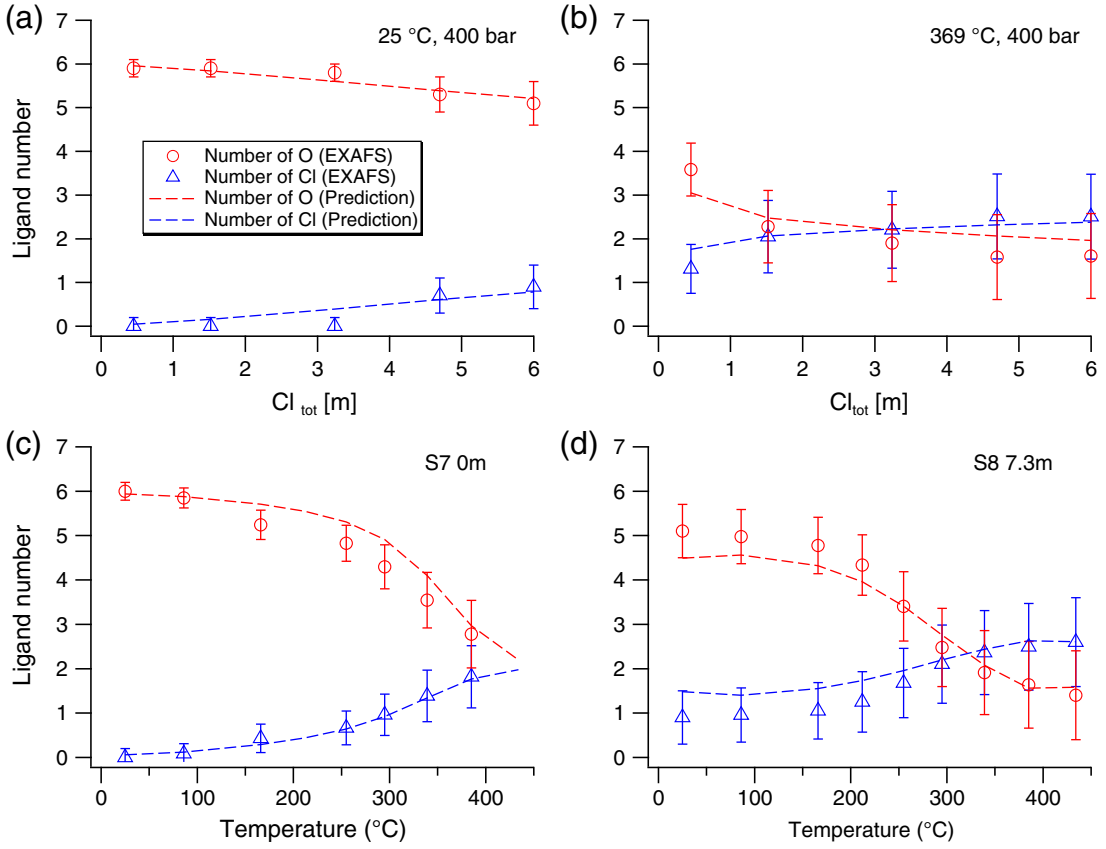

Fig. 6. Number of oxygen (water molecule; circles with error bars) and chloride (triangles with error bars) ligands in the first shell of Ni^{2+} as a function of chloride concentration at 25 °C (a) and 369 °C (b), and as a function of temperature for S7 (c) and S8 (d) based on the EXAFS refinements and the predictions of the thermodynamic model of Section 4.2 (dashed lines).

gives an explicit picture of the coordination changes of Ni(II) chloride complexes from ambient to hydrothermal conditions. Increasing T and/or chloride concentration favors the transition from a six-coordinated octahedral complex to a distorted four-coordinated tetrahedral complex.

At ambient conditions, chloride anions replace some water groups within the first octahedral shell with increasing Cl^- concentration (Table 3; Fig. 6a). The XANES spectra are sensitive to the break in symmetry introduced by the displacement of one H_2O molecule in $[Ni(H_2O)_6]^{2+}$

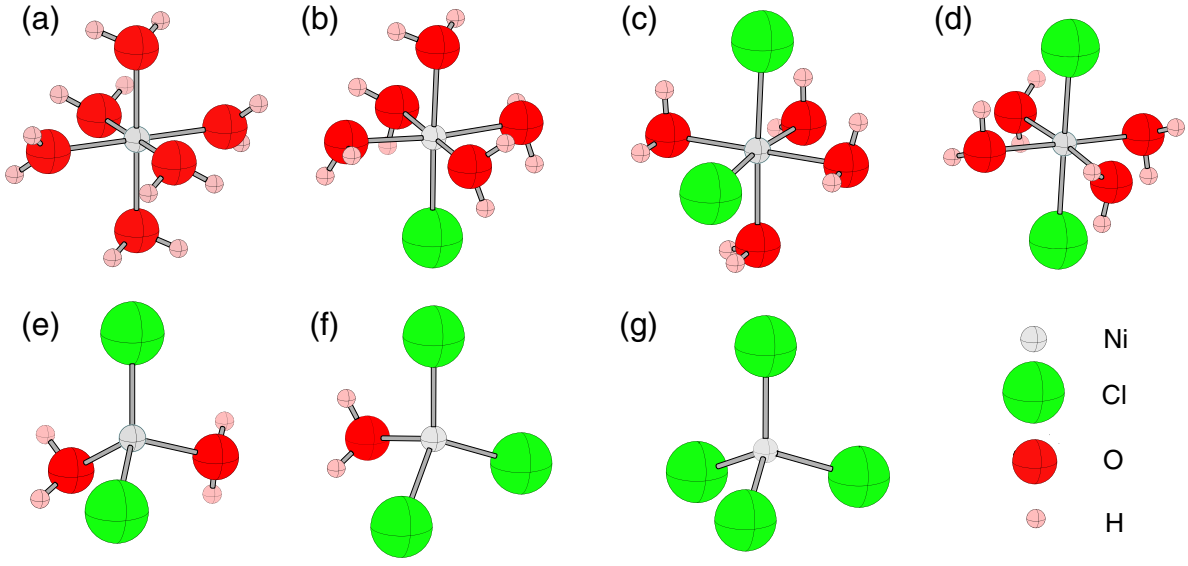

Fig. 7. Optimized geometries of Ni–Cl–H_2O clusters: (a) $Ni(H_2O)_6^{2+}$, (b) $NiCl(H_2O)_5^{+}$, (c) $NiCl_2(H_2O)_{4(aq)}$ (*cis*), (d) $NiCl_2(H_2O)_{4(aq)}$ (*trans*), (e) $NiCl_2(H_2O)_{2(aq)}$, (f) $NiCl_3(H_2O)^-$, (g) $NiCl_4^{2-}$.

Table 6
Geometries, Ni – O and Ni – Cl bond lengths (Å) and angles (°) of Nickel(II) clusters optimized by ADF program.

Ni Cluster	Geometry	$R_{(Ni-O)}$ (Å)	$R_{(Ni-Cl)}$ (Å)	$\Theta_{(Cl-Ni-Cl)}$	$\Theta_{(Cl-Ni-O)}$	$\Theta_{(O-Ni-O)}$
$Ni(H_2O)_6^{2+}$	Octahedral	2.08	–	–	–	90.00 90.00 86.21 93.79 90.00 90.00 90.00 90.00 90.00 90.00 86.21 93.79 180.00 180.00 180.00
$Ni(H_2O)_5Cl^+$	Octahedral	2.11	2.34	–	90.74 91.44 94.83 89.83 177.65	91.59 88.11 92.22 88.03 92.34 86.01 87.09 87.75 180.00 173.72
$Ni(H_2O)_4Cl_2$ (*cis*)	Octahedral	2.13	2.38	102.41	88.98 84.31 90.84 90.79 84.54 88.30 172.88 173.04	91.71 90.49 89.24 88.77 89.81 179.01
$Ni(H_2O)_4Cl_2$ (*trans*)	Octahedral	2.12	2.38	180.00	92.08 85.34 92.72 94.03 94.64 88.16 87.04 86.00	89.51 90.15 90.32 90.07 179.23 175.15
$Ni(H_2O)_2Cl_2$	Tetrahedral	2.04	2.22	144.81	95.70 101.09 99.69 109.05	98.23
$Ni(H_2O)Cl_3^-$	Tetrahedral	2.06	2.26	108.75 138.37 106.02	97.32 96.11 103.55	–
$NiCl_4^{2-}$	Tetrahedral	–	2.29	106.06 106.23 128.05 104.44 106.20 104.21	–	–

by one chloride, but further replacements of water molecules cause little change. Quantitative EXAFS refinements show that at 6 m Cl_{tot}, 0.9(0.5) Cl^- is bonded to Ni(II) (see Fig. 6a), indicating that the number of Cl ligands in these octahedral complexes $[NiCl_i(H_2O)_{6-i}]^{2-i}$ is unlikely to exceed 2 (i.e., $i \leq 2$). This is consistent with the predictions based on the thermodynamic properties of Liu et al. (2012b). In our speciation model the family of octahedral Ni–Cl–H_2O complexes at ambient conditions includes: $[Ni(H_2O)_6]^{2+}$, $[NiCl(H_2O)_5]^+$ and $[NiCl_2(H_2O)_4]_{(aq)}$. Species such as $[NiCl_3(H_2O)_3]^-$ and $[NiCl_4(H_2O)_2]^{2-}$ may exist in highly concentrated chloride solutions from room T to around 300 °C, but are likely to be only minor components (<10% of total Ni) and were not detectable in our system (salinity: 0 m–7.3 m) or in the UV-Vis experiments of Liu et al. (2012b). Note that a fully chlorinated octahedral $NiCl_6^{4-}$ species (125 °C, in a solution containing 22 m Cl^- introduced as $MgCl_2$) was proposed by Angell and Gruen (1966) on the basis of UV-Vis measurements. The discrepancy with our model might be due to the higher Cl^- concentrations; however, the stoichiometry and the number of species present in highly saline solutions are difficult to predict from UV-Vis measurements, because different salt concentrations cause distortions in the complexes that result in spectral differences (*i.e.*, deviations from the Beer-Lambert Law; Vinokurov and Kankare, 1998), that can be misinterpreted in terms of changing speciation (*e.g.*, Cu(II) chloride complexes, Brugger et al., 2001; Cu(I) chloride complexes, Liu et al., 2002; Brugger et al., 2007; Fe(III) chloride complexes, Liu et al., 2006).

With increasing T and/or salinity, the Ni^{2+} chlorocomplexes exhibit a change in coordination from octahedral to tetrahedral. This coordination change is in good agreement with the dehydration process around Ni^{2+} in a 2 m $NiCl_2$ heavy water solution from 100 to 300 °C at 1000 bar (Jong et al., 1996) and with the structural transition of Ni–Br–H_2O complexes from ambient to supercritical conditions (Wallen et al., 1998; Hoffmann et al., 1999). By means of XAS, NIR spectroscopy and MD studies, Hoffmann et al. (1999) identified a family of four-coordinated species: $[NiBr(H_2O)_3]^+$, $[NiBr_2(H_2O)_2]_{(aq)}$ and $[NiBr_3(H_2O)]^-$, but found no evidence for a fully halogenated complex, $[NiBr_4]^{2-}$. Our XANES and EXAFS data analyses show a similar behavior for the Ni(II) chloride complexes, with speciation at elevated temperatures (≥400 °C) mainly consisting of two tetrahedral complexes: $[NiCl_2(H_2O)_2]_{(aq)}$ and $[NiCl_3(H_2O)]^-$, and no evidence for the fully chlorinated $[NiCl_4]^{2-}$ complex. The selected $[NiCl_2(H_2O)_2]_{(aq)}$ and $[NiCl_3(H_2O)]^-$ complexes are also consistent with the species identified by Lüdemann and Franck (1968) using UV-Vis spectrophotometry, and by Lin and Popp (1984), Fahlquist and Popp (1989) and Uchida et al. (1996) *via* solubility experiments.

4.2. Thermodynamic analysis and comparison with previous studies

A number of (distorted) octahedral and tetrahedral Ni(II) chlorocomplexes exist in our experimental solutions over the range of temperatures and chlorinities investigated. In some cases, it is possible to retrieve formation constants of aqueous chloride complexes from XANES data (*e.g.*, Liu et al., 2007; Testemale et al., 2009; Etschmann et al., 2011; Liu et al., 2011, 2012a). In the case of Ni(II) chloride complexes, however, fitting was unstable, resulting in poor convergence, multiple minima, and/or unrealistic spectra for the individual complexes. This is partly because of the limited number of spectra (5) at each temperature. Principal component analysis reveals that two components explain >99.7% of the variance of the 400 bar dataset; the Ni(II) chloride system is hence severely underconstrained. In other cases (*e.g.*, Co(II)-chlorides; Liu et al., 2011), additional constraints (*e.g.*, mass balance and mass action equations) enabled the retrieval of stability constants. In the case of Ni(II), however, the concentration profiles and individual spectra of many species appear to be highly correlated, and several species occur only in small concentrations. Another major potential problem is that $NiCl_{2(aq)}$ is a significant species at low temperature as well as at high temperature (Fig. 11), based on recent UV-Vis and solubility studies (Lin and Popp, 1984; Liu et al., 2012b). However, XAS data clearly indicate that at temperatures ≤174 °C, Ni(II) species exist predominantly as octahedral complexes, while at ≥312 °C, most of the Ni(II) is present as tetrahedral complexes. This strongly suggests that both tetrahedral (T_d) and octahedral (O_h) $NiCl_{2(aq)}$ complexes are important for Ni(II) speciation, the former becoming the predominant form at high temperature. Since both complexes have the same number of Cl ions, they vary in a perfectly correlated manner as a function of salt concentration (*e.g.*, Fig. 11b), causing strong numerical problems for the thermodynamic analysis of the XANES data.

In view of these difficulties, we chose to limit our analysis to showing that our XANES and EXAFS data are consistent with the model proposed recently by Liu et al. (2012b). Liu et al. (2012b) fitted the formation constants for the Ni(II) complexes $NiCl_x$ (x = 1–3) based on UV-Vis data collected at 25–250 °C and P = 100 bar, and combined these new data with the high temperature, high pressure solubility data of Lin and Popp

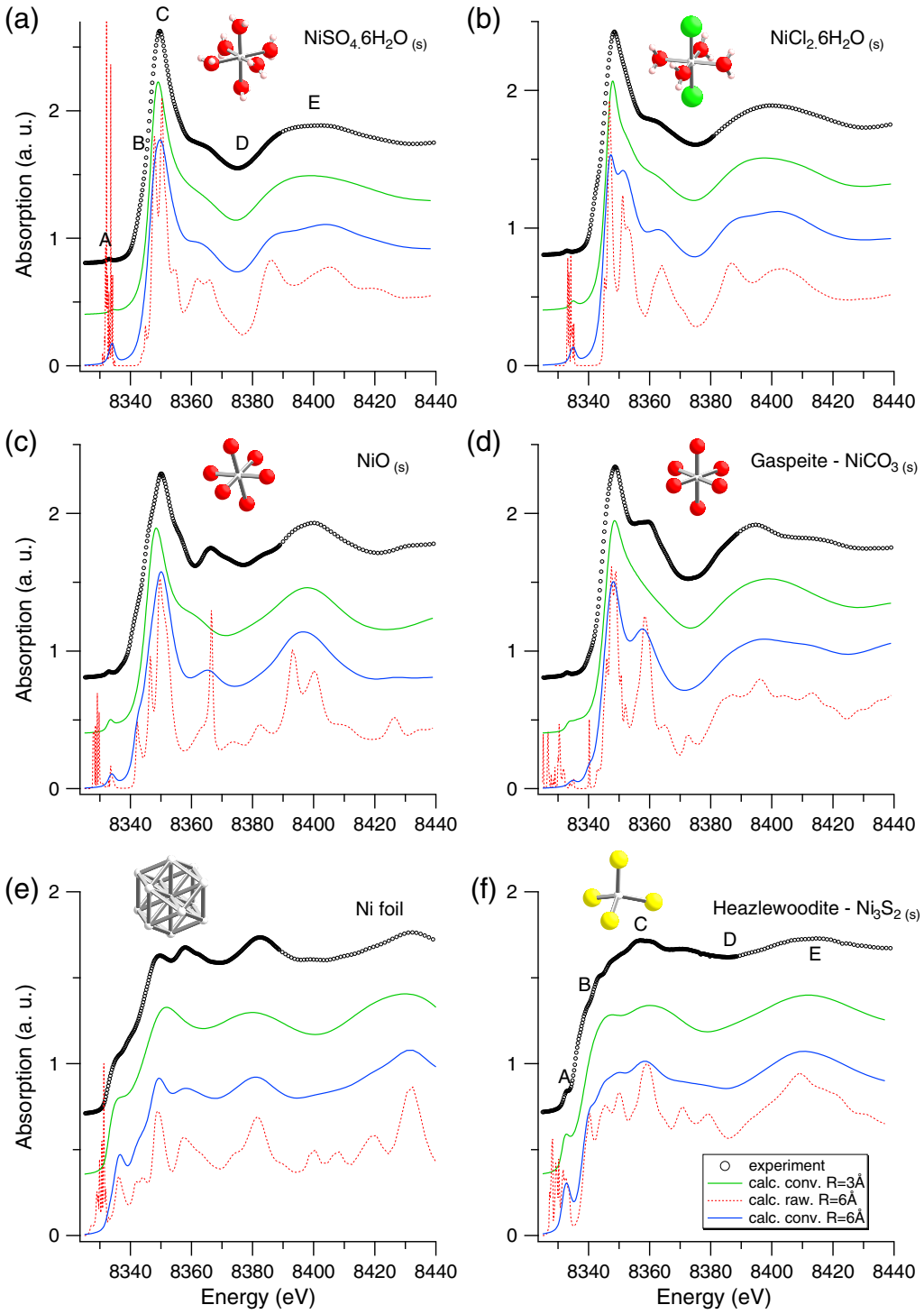

Fig. 8. Experimental and calculated (both raw and convoluted) XANES spectra for Ni model compounds. Open circle: experimental spectra; green line: convoluted spectra calculated within a cluster size of 3 Å; blue line: convoluted spectra calculated within a cluster size of 6 Å; red dotted line: calculated raw spectra within a cluster size of 6 Å. Crystal structures used for the calculations: (a) Rousseau et al. (2000); (b) Kleinberg (1969); (c) Sasaki et al. (1979); (d) Pertlik (1986); (e) Suh et al. (1988); (f) Parise (1980).

(1984) and Fahlquist and Popp (1989) (450–750 °C, 1–2 kbar) into a consistent dataset using the modified Ryzhenko–Bryzgalin (MRB) model (Ryzhenko et al., 1985). Liu et al. (2012b) fitted the properties of $NiCl_{2(aq)}$ at each temperature, and the $NiCl_{2(aq)}$ concentrations were calculated using their properties hence effectively represent the sum of the octahedral and tetrahedral forms of the complex, *i.e.*

$$[NiCl_2(aq)] = {}^{Td}[NiCl_2(H_2O)_2(aq)] + {}^{Oh}[NiCl_2(H_2O)_4(aq)] \quad (1)$$

In terms of formation constants for the complexes, this means that:

$$k_{NiCl_{2(aq)}} = \frac{a_{NiCl_{2(aq)}}\left[NiCl_{2(aq)}\right]}{a_{Ni^{2+}}\left[Ni^{2+}\right]a_{Cl^-}^2\left[Cl^-\right]^2} = k_{T_d} + k_{O_h}, \quad (2)$$

assuming that $\gamma_{NiCl_2(aq)} = \gamma_{T_d[NiCl_2(H_2O)_2(aq)]} = \gamma_{O_h[NiCl_2(H_2O)_4(aq)]}$.

Therefore, the only thermodynamic parameter that we refined was k_{Oh}, and k_{Td} was then determined according to Eq. (2). We fitted the

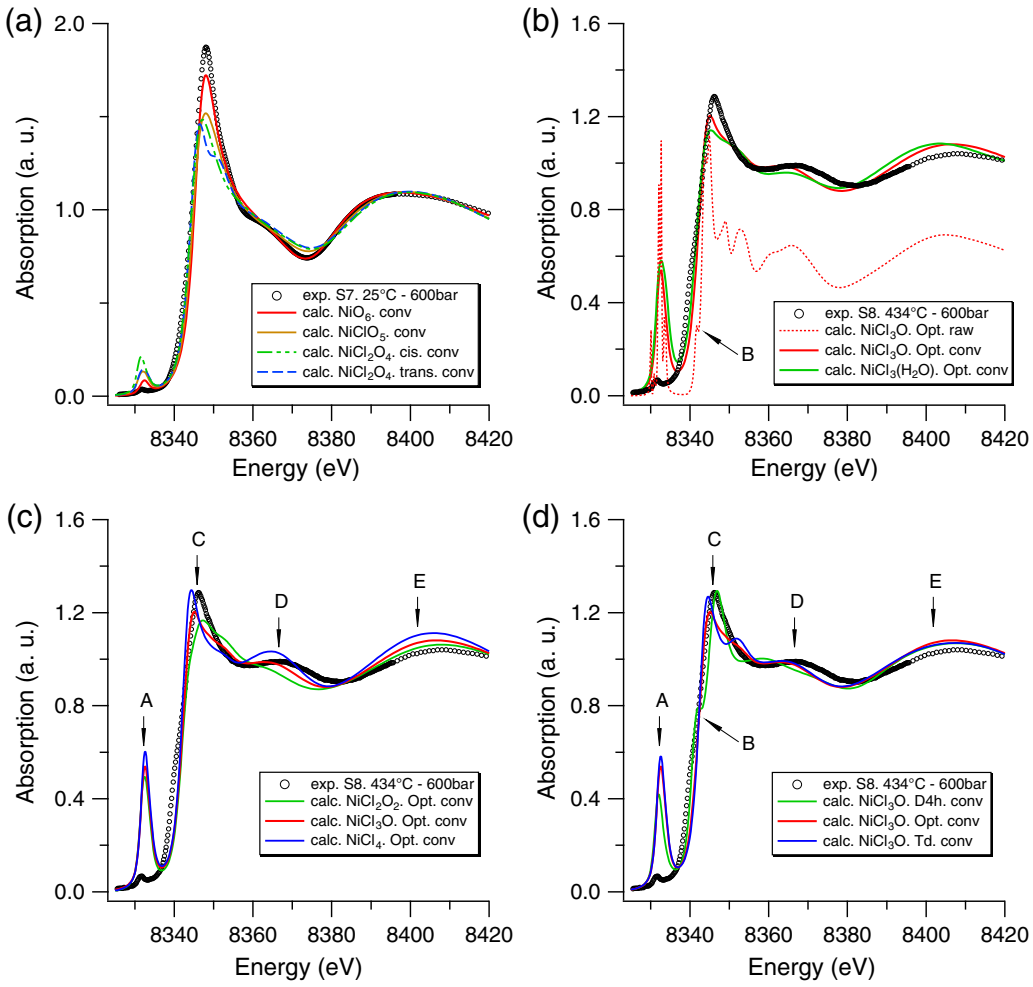

Fig. 9. Experimental and calculated XANES spectra of Ni aqueous species: (a) octahedral NiO_6, $NiClO_5$ and $NiCl_2O_4$; (b) tetrahedral $NiCl_3O$ and $NiCl_3(H_2O)$; (c) DFT optimized $NiCl_2O_2$, $NiCl_3O$ and $NiCl_4$; (d) $NiCl_3O$ with square planar (D_{4h}), DFT optimized (Opt) and regular tetrahedral (T_d) geometries.

XANES spectra at 400 bar using the BeerOz package (Brugger, 2007). Essentially, the measured normalized XANES spectra are the sum of the contributions of each Ni(II) complex present in solution (*e.g.*, Brugger, 2007; Liu et al., 2012a):

$$\tilde{A}_\lambda = \sum_{i=1}^{n} x_i \tilde{\varepsilon}_{i,\lambda} \quad (3)$$

$$x_i = \frac{m_{NiCl_i(H_2O)_{n-i}^{2-i}}}{\sum_i m_{Ni,total}} \quad (4)$$

where $\tilde{\varepsilon}_{i,\lambda}$ is the normalized absorbance at wavelength λ; $\tilde{A}_\lambda$ is the normalized absorbance of the i^{th} contributing species; x_i is the mole fraction of each Ni complex present in solution; $m_{NiCl_i(H_2O)_{n-i}^{2-i}}$ is the molality of the subscribed complex; and n is the coordination number of the complex (6 for octahedral species and 4 for tetrahedral species). The assumption that the XANES spectra of individual Ni complexes are constant over the temperature and concentration range of their predominance is supported by the fact that such distortions have been observed only for open structures that are predominant over wide ranges of conditions (*e.g.*, $CuCl_3^{2-}$, Brugger et al., 2007; $As(OH)_{3(aq)}$, Testemale et al., 2004). In addition, *ab initio* XANES calculations show that the XANES spectra are not very sensitive to small changes in bond distances and geometry (see *e.g.* Testemale et al., 2009 for similar calculations of octahedral and tetrahedral Fe(II) chlorocomplexes; Bazarkina et al., 2010 for Cd(II) chlorocomplexes).

In the first round, we considered the first four datasets (from 25 to 174 °C), and assumed that only the octahedral species Ni^{2+}, $NiCl^+$ and $NiCl_{2(aq)}$ were present. The only free parameters were the individual spectra of these three octahedral species. In the next round, we fixed the individual spectra of the octahedral species Ni^{2+} and $NiCl^+$ to those obtained in the previous step, and refined the individual spectra of octahedral $NiCl_{2(aq)}$ and tetrahedral $NiCl_{2(aq)}$ and the T_d/(total ratio of the $NiCl_{2(aq)}$ species) based over the whole dataset (25 to 369 °C). Two tetrahedral complexes were present in the model: $[NiCl_2(H_2O)_2]_{(aq)}$ and $[NiCl_3(H_2O)]^-$. Where the spectra of both tetrahedral complexes were refined, $[NiCl_3(H_2O)]^-$ had a spectrum that did not resemble a valid XANES spectrum. Hence we decided to fix the spectrum of this complex to be equal to that of solution S8 at 434 °C and 600 bar, for which the XANES and XANES analyses indicate that $[NiCl_3(H_2O)]^-$ is the predominant species.

The results of the analysis are shown in Figs. 10 and 11 and the log K used in the analysis is listed together with the fitted values in Table 7. Comparison of the BeerOz-extracted spectra of each individual Ni species to those calculated by the FDMNES program reveals a good agreement of the spectral features (Fig. 10a). In particular the spectral evolution for Ni octahedral species with increasing number of chloride follows the trend predicted by the XANES simulations (Fig. 10a). The extracted XANES spectra of T_d $[NiCl_2(H_2O)_2]_{(aq)}$ and O_h $[NiCl_2(H_2O)_4]_{(aq)}$ have similar shapes of the white line, but they differ

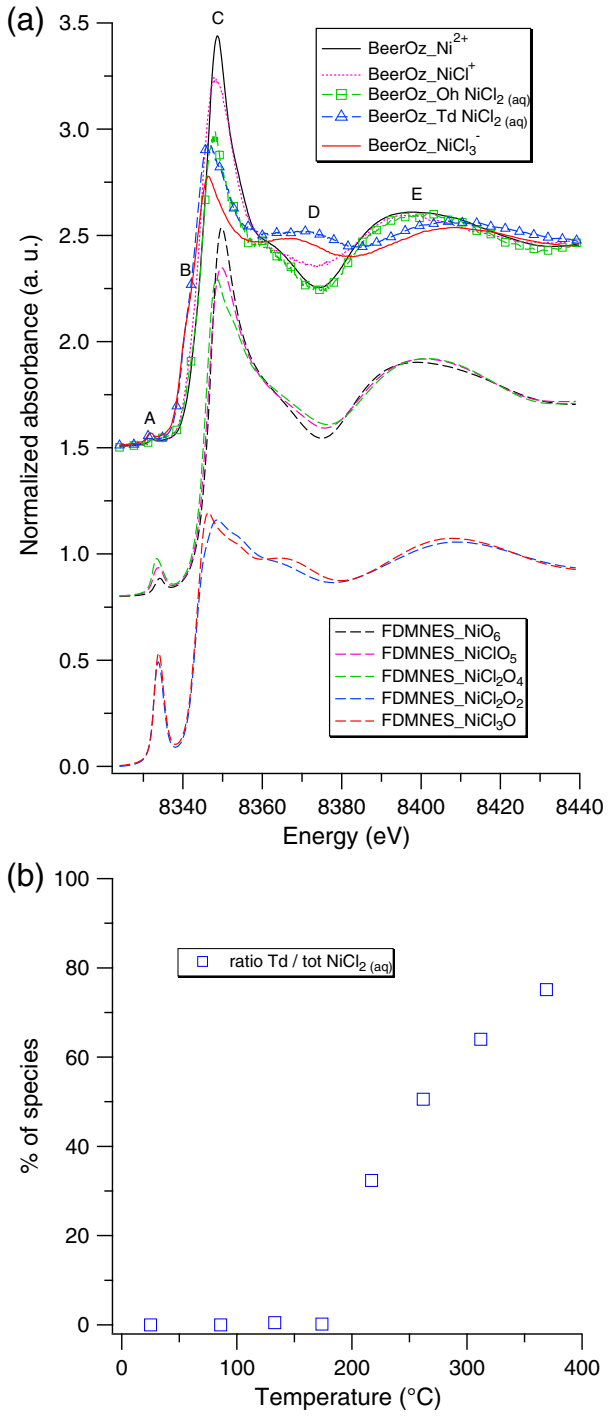

Fig. 10. Results of fitting of XANES data using the speciation model of Liu et al. (2012b): (a) calculated spectra of each individual species and compared with those calculated by FDMNES program; (b) ratio of tetrahedral $NiCl_2(H_2O)_{2(aq)}$ to total $NiCl_{2(aq)}$.

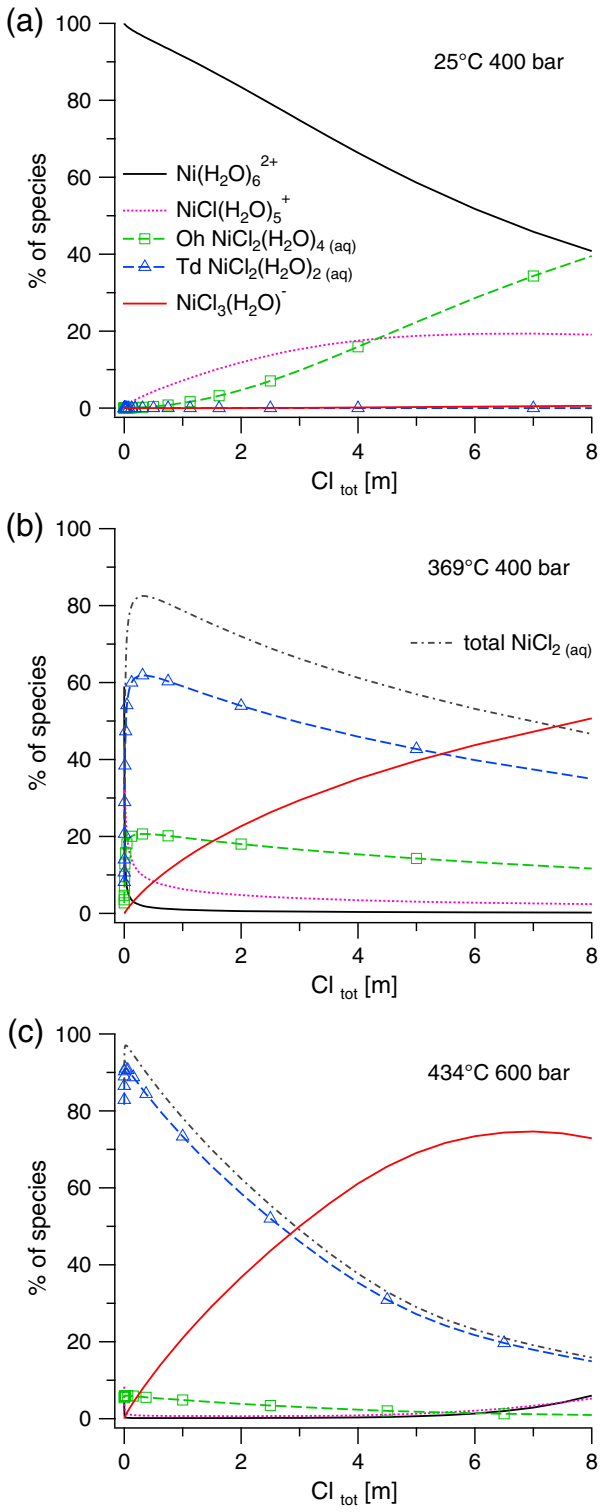

Fig. 11. Speciation as a function of salinity according to the refined thermodynamic properties based on those of Liu et al. (2012b) at (a) 25 °C 400 bar, (b) 369 °C 400 bar, and (c) 434 °C 600 bar. The nickel concentration used in this plot was 0.1 mmolal.

from each other in terms of the absence of the B-shoulder in the octahedral complex, the position of the white line, the position and intensity of the D feature, and the position of the E feature, all typical spectral differences between tetrahedral and octahedral complexes. The fitting reveals that the ratio of T_d $NiCl_{2(aq)}$ to O_h $NiCl_{2(aq)}$ increases steadily above 200 °C (Fig. 10b). Furthermore, the average number of water and chloride ligands as a function of salinity (25 °C and 369 °C, 400 bar) and as a function of temperature (S7 and S8, 600 bar) calculated using the resulting speciation model was in excellent agreement with those retrieved by EXAFS refinements (see Fig. 6), which supports the choice of speciation model and thermodynamic analysis.

The speciation of Ni(II) as a function of chloride concentration at 25 °C–400 bar, 369 °C–400 bar and 434 °C–600 bar calculated using the thermodynamic properties of Liu et al. (2012b) as well as the T_d and O_h fractions of $NiCl_{2(aq)}$ are shown in Fig. 11. The 25 °C diagram

Table 7
Formation constants of the aqueous species at 400 bar used in thermodynamic analysis.

Species	25 °C	91 °C	133 °C	174 °C	217 °C	262 °C	312 °C	369 °C	References
$HCl_{(aq)}$	−0.71	−0.93	−0.77	−0.48	−0.09	0.42	1.11	2.03	Extrapolated from Tagirov et al. (1997)
$NaCl_{(aq)}$	−0.83	−0.56	−0.37	−0.15	0.10	0.41	0.85	1.44	Extrapolated from Sverjensky et al. (1997)
$NiCl^{+}$	−1.03	−0.67	−0.36	−0.02	0.37	0.84	1.46	2.15	Extrapolated from Sverjensky et al. (1997)
	−0.48	0.03	0.36	0.69	1.04	1.43	1.93	2.70	Extrapolated from Liu et al. (2012b)
$NiCl_{2(aq)}$	−0.89	−0.70	−0.24	0.37	1.13	2.05	3.26	5.14	Extrapolated from Liu et al. (2012b)
$NiCl_2(H_2O)_{4(aq)}$	−0.89	−0.70	−0.24	0.37	0.96	1.74	2.81	4.54	Fitted in this study
$NiCl_2(H_2O)_{2(aq)}$	−6.89	−6.70	−2.55	−2.42	0.64	1.75	3.06	5.02	Fitted in this study
$NiCl_3^{-}$	−3.38	−2.84	−2.13	−1.28	−0.27	0.92	2.44	4.74	Extrapolated from Liu et al. (2012b)

Table 8
Revised Ryzhenko parameters ($A(zz/a)$ and $B(zz/a)$) for O_h $NiCl_2(H_2O)_{4(aq)}$ and T_d $NiCl_2(H_2O)_{2(aq)}$.

MRB parameters	log $K_{(298)}$	$A_{(zz/a)}$	$B_{(zz/a)}$
O_h $NiCl_2(H_2O)_{4(aq)}$	−0.953	2.095	−718.9
T_d $NiCl_2(H_2O)_{2(aq)}$	−5.618	2.104	−369.5

indicates that no tetrahedral species is present at room temperature, and increasing chlorinity favors replacement of water molecules by chloride ligands around Ni^{2+}; the 369 °C diagram shows that octahedral species still persist in equilibrium with tetrahedral species at 369 °C. The last two diagrams suggest that tetrahedral species predominate in the whole salinity range at 434 °C, 600 bar, and increasing salinity favors the formation of $NiCl_3^{-}$, which is believed to play an important role in Ni transport in Cl-rich hydrothermal fluids under these conditions.

The formation constants of O_h $[NiCl_2(H_2O)_4]_{(aq)}$ from 25 °C to 369 °C at 400 bar refined in this study were used to fit Ryzhenko–Bryzgalin (MRB) model parameters (Ryzhenko et al., 1985) using the OptimC program (Shvarov, 2008). The Ryzhenko–Bryzgalin equation is a simple extrapolation method that allows description of the change of stability constant as a function of pressure and temperature based on the room-T log K and two adjustable parameters (Table 8). For T_d $[NiCl_2(H_2O)_2]_{(aq)}$, the experimental formation constants derived from the solubility study by Lin and Popp (1984) from 450 °C to 650 °C at 1 kbar and 2 kbar were taken into account besides the data refined in this study, assuming that the $NiCl_{2(aq)}$ species of Lin and Popp (1984) is T_d $[NiCl_2(H_2O)_2]_{(aq)}$. As T_d $[NiCl_2(H_2O)_2]_{(aq)}$ is not detectable at low temperature, a weighting of 1 was used for all the data at temperature ≥217 °C with a weighting of 0.25 and 0.5 used for data at 25–91 °C and at 133–174 °C, respectively. The log K values for O_h $[NiCl_2(H_2O)_4]_{(aq)}$, T_d $[NiCl_2(H_2O)_2]_{(aq)}$ and the total $NiCl_{2(aq)}$ (sum of the formation constants for O_h $[NiCl_2(H_2O)_4]_{(aq)}$, T_d $[NiCl_2(H_2O)_2]_{(aq)}$, Eq. (2)) at 1 kbar calculated using these new parameters are shown in Fig. 12.

4.3. Comparison to Co chloride complexes

The XANES spectra of aqueous Ni–Cl–H_2O complexes exhibit analogous changes as other first row divalent transition metals (*e.g.*, Fe, Co, Zn, Cu; Fulton et al., 2000; Liu et al. 2007, 2011, 2012a; Testemale et al., 2009). Increasing temperature leads to a reduction in the coordination number of the complex (in effect a dehydration reaction), and increasing chlorinity favors the replacement of water by chloride anions in particular leading to chloride-rich tetrahedral complexes at high temperature (*i.e.*, 369 °C). Hence, the stability of tetrahedral complexes relative to octahedral complexes is promoted by both heating and increase in chloride concentrations. Compared to Co(II), the octahedral to tetrahedral coordination change occurs at higher temperature for Ni(II) complexes, Co(II) being fully tetrahedral at 250 °C in a 6.05 m Cl^{-} solution (Cl:Co molar ratio at 106; Liu et al., 2011). Also, for Co(II), the fully chlorinated tetrahedral complex $[CoCl_4]^{2-}$ is very stable, being the dominant species in concentrated brines at elevated temperature. In contrast, the highest order Ni complex characterized experimentally here, distorted tetrahedral $[NiCl_3(H_2O)]^{-}$, is not fully chlorinated. Further studies, in particular molecular dynamics simulations, need to be done to reveal the cause of the different behavior of

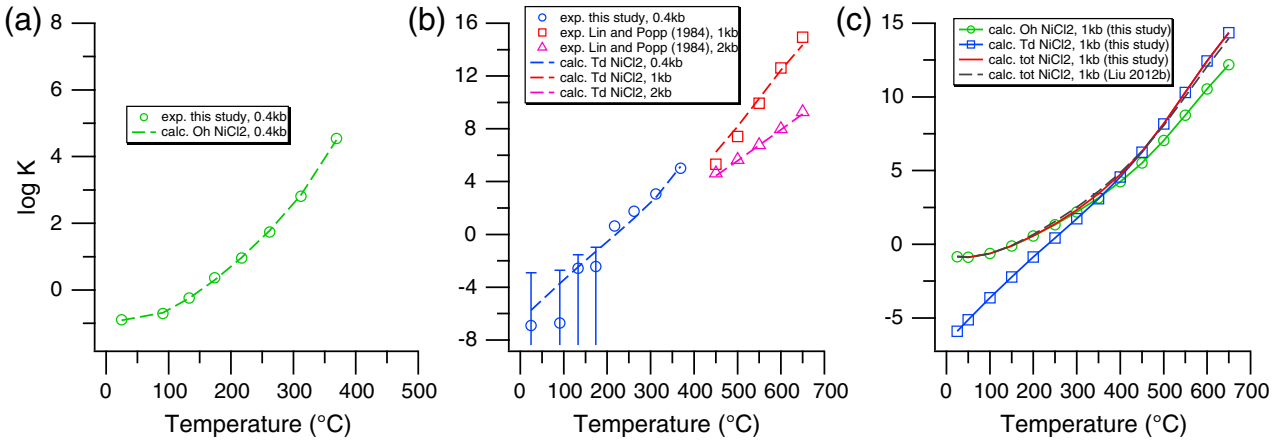

Fig. 12. (a) Formation constants (log K) for Oh $[NiCl_2(H_2O)_4]_{(aq)}$ determined by BeerOz in this study and theoretical calculation using the Ryzhenko parameters of Oh $[NiCl_2(H_2O)_4]_{(aq)}$ listed in Table 8; (b) Formation constants (log K) for Td $[NiCl_2(H_2O)_2]_{(aq)}$ determined by BeerOz in this study and by Lin and Popp (1984) and theoretical calculation using the Ryzhenko parameters of Td $[NiCl_2(H_2O)_2]_{(aq)}$ listed in Table 8; (c) Theoretical calculation using the Ryzhenko parameters of Oh $[NiCl_2(H_2O)_4]_{(aq)}$ and Td $[NiCl_2(H_2O)_2]_{(aq)}$ listed in Table 8 at 1 kbar, with the total $NiCl_{2(aq)}$ of this study and that of Liu et al. (2012b) also shown for comparison.

Ni and Co complexes. Such differences can explain the sharp contrast in mobility of Ni and Co in hydrothermal brines, with much of the World's cobalt resources found in hydrothermal deposits while the vast majority of Ni resources are mined from magmatic deposits and their broadly *in situ* weathering products.

Acknowledgments

This research was undertaken on the XAS beamline at the Australian Synchrotron, Victoria, Australia. Research funding was provided by Australian Research Council (ARC) to JB (DP0878903), and the Minerals Down Under Flagship to WL. The mAESTRO system was designed and constructed as a part of a LIEF grant (LE0882493) by the University of Adelaide and CSIRO in collaboration with CNRS scientists. The FDMNES calculation was supported by iVEC through the use of the EPIC advanced computing resource located in Perth, Australia. YT acknowledges the University of Adelaide for an ASI scholarship. The paper benefited from comments by J. Fein, A. Migdisov, and an anonymous reviewer.

References

Almeida, C.M., Olivo, G.R., Carvalho, S.G., 2007. The Ni–Cu–PGE sulfide ores of the komatiite-hosted Fortaleza de Minas deposit, Brazil: evidence of hydrothermal remobilization. The Canadian Mineralogist 45, 751–773.

Angell, C.A., Gruen, D.M., 1966. Octahedral–tetrahedral coordination equilibria of nickel(II) and copper(II) in concentrated aqueous electrolyte solutions. Journal of the American Chemical Society 88, 5192–5198.

Ankudinov, A.L., Ravel, B., Rehr, J.J., Conradson, S.D., 1998. Real-space multiple-scattering calculation and interpretation of X-ray-absorption near-edge structure. Physics Review B 58, 7565–7576.

Barnes, S.-J., Lightfoot, P.C., 2005. Formation of magmatic nickel-sulfide ore deposits and processes affecting their copper and platinum-group element contents. In: Hedenquist, J.W., Thompson, J.F.H., Goldfarb, R.J., Richards, J.P. (Eds.), Economic Geology, pp. 179–213 (100th Anniversary Volume).

Barnes, S.J., Liu, W., 2012. Pt and Pd mobility in hydrothermal fluids: evidence from komatiites and from thermodynamic modelling. Ore Geology Reviews 44, 49–58.

Bazarkina, E.F., Pokrovski, G.S., Zotov, A.V., Hazemann, J.-L., 2010. Structure and stability of cadmium chloride complexes in hydrothermal fluids. Chemical Geology 276, 1–17.

Brugger, J., 2007. BeerOz, a set of Matlab routines for the quantitative interpretation of spectrophotometric measurements of metal speciation in solution. Computers and Geosciences 33, 248–261.

Brugger, J., Black, J., McPhail, D.C., Spiccia, L., 2001. UV-Vis-NIR spectroscopic study of Cu(II) complexing in LiCl brines between 20 and 90 °C. Geochimica et Cosmochimica Acta 65, 2691–2708.

Brugger, J., Etschmann, B., Liu, W., Testemale, D., Hazemann, J.L., Emerich, H., van Beek, W., Proux, O., 2007. An XAS study of the structure and thermodynamics of Cu(I) chloride complexes in brines up to high temperature (400 °C, 600 bar). Geochimica et Cosmochimica Acta 71, 4920–4941.

Brugger, J., Pring, A., Reith, F., Ryan, C., Etschmann, B., Liu, W., O'Neill, B., Ngothai, Y., 2010. Probing ore deposits formation: new insights and challenges from synchrotron and neutron studies. Radiation Physics and Chemistry 79, 151–161.

Bruyère, R., Prat, A., Goujon, C., Hazemann, J.-L., 2008. A new pressure regulation device using high pressure isolation valves. Journal of Physics Conference Series 121, 122003.

Chen, Y., Fulton, J., Partenheimer, W., 2005a. A XANES and EXAFS study of hydration and ion pairing in ambient aqueous $MnBr_2$ solutions. Journal of Solution Chemistry 34, 993–1007.

Chen, Y., Fulton, J.L., Partenheimer, W., 2005b. The structure of the homogeneous oxidation catalyst, Mn(II)(Br-1)x, in supercritical water: an X-ray absorption fine-structure study. Journal of the American Chemical Society 127, 14085–14093.

D'Angelo, P., Roscioni, O.M., Chillemi, G., Della Longa, S., Benfatto, M., 2006. Detection of second hydration shells in ionic solutions by XANES: computed spectra for Ni^{2+} in water based on molecular dynamics. Journal of the American Chemical Society 128, 1853–1858.

de Groot, F., Vanko, G., Glatzel, P., 2009. The 1s X-ray absorption pre-edge structures in transition metal oxides. Journal of Physics: Condensed Matter 21.

Driesner, T., Heinrich, C.A., 2007. The system H2O-NaCl. Part I: correlation formulae for phase relations in temperature-pressure-composition space from 0 to 1000 °C, 0 to 5000 bar, and 0 to 1 XNaCl. Geochimica et Cosmochimica Acta 71, 4880–4901.

Driesner, T., 2007. The system H2O-NaCl. Part II: correlations for molar volume, enthalpy, and isobaric heat capacity from 0 to 1000 °C, 1 to 5000 bar, and 0 to 1 XNaCl. Geochimica et Cosmochimica Acta 71, 4902–4919.

Etschmann, B.E., Liu, W., Testemale, D., Müller, H., Rae, N.A., Proux, O., Hazemann, J.L., Brugger, J., 2010. An in situ XAS\ study of copper(I) transport as hydrosulfide complexes in hydrothermal solutions (25–592 °C, 180–600 bar): speciation and solubility in vapor and liquid phases. Geochimica et Cosmochimica Acta 74, 4723–4739.

Etschmann, B.E., Black, J.R., Grundler, P.V., Borg, S., Brewe, D., McPhail, D.C., Spiccia, L., Brugger, J., 2011. Copper(I) speciation in mixed thiosulfate-chloride and ammonia-chloride solutions: XAS and UV-Visible spectroscopic studies. RSC Advances 1, 1554–1566.

Fahlquist, L.S., Popp, R.K., 1989. The effect of NaCl on bunsenite solubility and Ni-complexing in supercritical aqueous fluids. Geochimica et Cosmochimica Acta 53, 989–995.

Fan, R., Gerson, A.R., 2011. Nickel geochemistry of a Philippine laterite examined by bulk and microprobe synchrotron analyses. Geochimica et Cosmochimica Acta 75, 6400–6415.

Farges, F., Brown Jr., G.E., Petit, P.-E., Munoz, M., 2001a. Transition elements in water-bearing silicate glasses/melts. Part I. A high-resolution and anharmonic analysis of Ni coordination environments in crystals, glasses, and melts. Geochimica et Cosmochimica Acta 65, 1665–1678.

Farges, F., Munoz, M., Siewert, R., Malavergne, V., Brown Jr., G.E., Behrens, H., Nowak, M., Petit, P.-E., 2001b. Transition elements in water-bearing silicate glasses/melts. Part II. Ni in water-bearing glasses. Geochimica et Cosmochimica Acta 65, 1679–1693.

Fernandez, D.P., Goodwin, A.R.H., Lemmon, E.W., Sengers, J.M.H.L., Williams, R.C., 1997. A Formulation for the Static Permittivity of Water and Steam at Temperatures from 238 K to 873 K at Pressures up to 1200 MPa, Including Derivatives and Debye-Hückel Coefficients. Journal of Physical and Chemical Reference Data 26, 1125–1166.

Fulton, J.L., Hoffmann, M.M., Darab, J.G., Palmer, B.J., Stern, E.A., 2000. Copper(I) and copper(II) coordination structure under hydrothermal conditions at 325 °C: an X-ray absorption fine structure and molecular dynamics study. Journal of Physical Chemistry A 104, 11651–11663.

Fulton, J.L., Heald, S.M., Badyal, Y.S., Simonson, J.M., 2003. Understanding the effects of concentration on the solvation structure of Ca^{2+} in aqueous solution. I: the perspective on local structure from EXAFS and XANES. Journal of Physical Chemistry A 107, 4688–4696.

Galoisy, L., Calas, G., 1993. Structural environment of nickel in silicate glass/melt systems: Part 1. Spectroscopic determination of coordination states. Geochimica et Cosmochimica Acta 57, 3613–3626.

Harald, G.D., 2010. The "chessboard" classification scheme of mineral deposits: mineralogy and geology from aluminum to zirconium. Earth-Science Reviews 100, 1–420.

Hayter, R.G., Humiec, F.S., 1965. Square-planar-tetrahedral isomerism of nickel halide complexes of diphenylalkylphosphines. Inorganic Chemistry 4, 1701–1706.

Hoffmann, M.M., Darab, J.G., Palmer, B.J., Fulton, J.L., 1999. A transition in the Ni^{2+} complex structure from six- to four-coordinate upon formation of ion pair species in supercritical water: an X-ray absorption fine structure, near-infrared, and molecular dynamics study. Journal of Physical Chemistry A 103, 8471–8482.

Joly, Y., Cabaret, D., Renevier, H., Natoli, C.R., 1999. Electron Population Analysis by Full-Potential X-Ray Absorption Simulations. Physical Review Letters 82, 2398.

Joly, Y., 2001. X-ray absorption near-edge structure calculations beyond the muffin-tin approximation. Physics Review B 63, 125120.

Jong, P.H.K., Neilson, G.W., Bellissent-Funel, M.-C., 1996. Hydration of Ni^{2+} and Cl^{-} in a concentrated nickel chloride solution at 100 °C and 300 °C. Journal of Chemical Physics 105, 5155–5159.

Keays, R.R., Jowitt, S.M., Callaghan, T., 2009. The Avebury Ni deposit, Tasmania: a case study of an unconventional nickel deposit. In: Williams, P.J. (Ed.), Smart Science for Exploration and Mining: Proceedings of the Tenth Biennial SGA Meeting, Townsville.

Kelly, S.D., Hesterberg, D., Ravel, B., 2008. Analysis of soils and minerals using X-ray absorption spectroscopy. In: Ulery, A.L., Drees, L.R. (Eds.), Methods of Soil Analysis. Part 5. Mineralogical Methods. SSSA Book Series No. 5, pp. 387–483.

Kissin, S.A., 1992. Five-element (Ni-Co-As-Ag-Bi) veins. Geoscience Canada 19, 113–124.

Klamt, A., Schuurmann, G., 1993. COSMO: a new approach to dielectric screening in solvents with explicit expressions for the screening energy and its gradient. Journal of the Chemical Society, Perkin Transactions 2, 799–805.

Kleinberg, R., 1969. Crystal structure of $NiCl_2.6H_2O$ at room temperature and 4.2°K by neutron diffraction. Journal of Chemical Physics 50, 4690–4696.

Krause, M.O., Oliver, J.H., 1979. Natural widths of atomic *K* and *L* levels, Kα X-ray lines and several KLL Auger lines. Journal of Physical and Chemical Reference Data 8, 329–338.

Krill, G., Amamou, A., 1980. XPS and UPS studies of pyrite compounds ($CoX2 \rightarrow CuX2$, *X*: S; Se): investigation of the insulator-metal transition in the $NiS_{2-x}Se_x$ system. Journal of Physics and Chemistry of Solids 41, 531–538.

Lemmon, E.W., McLinden, M.O., Friend, D.G., 2000. Thermophysical properties of fluid systems. In: Mallard, W.G., Linstrom, P.J. (Eds.), NIST Chemistry WebBook, NIST Standard Reference Database. National Institute of Standards and Technology, Gaithersburg, MD (Available from: http://webbook.nist.gov).

Lin, S., Popp, R.K., 1984. Solubility and complexing of Ni in the system NiO–H_2O–HCl. Geochimica et Cosmochimica Acta 48, 2713–2722.

Liu, W., Brugger, J., McPhail, D.C., Spiccia, L., 2002. A spectrophotometric study of aqueous copper(I)–chloride complexes in LiCl solutions between 100 °C and 250 °C. Geochimica et Cosmochimica Acta 66, 3615–3633.

Liu, W., Etschmann, B., Brugger, J., Spiccia, L., Foran, G., McInnes, B., 2006. UV-Vis spectrophotometric and XAFS studies of ferric chloride complexes in hyper-saline LiCl solutions at 25–90 °C. Chemical Geology 231, 326–349.

Liu, W., Etschmann, B., Foran, G., Shelley, M., Brugger, J., 2007. Deriving formation constants for aqueous metal complexes from XANES spectra: Zn^{2+} and Fe^{2+} chloride complexes in hypersaline solutions. American Mineralogist 92, 761–770.

Liu, W., Borg, S.J., Testemale, D., Etschmann, B., Hazemann, J.-L., Brugger, J., 2011. Speciation and thermodynamic properties for cobalt chloride complexes in hydrothermal fluids at 35–440 °C and 600 bar: an in-situ XAS study. Geochimica et Cosmochimica Acta 75, 1227–1248.

Liu, W., Borg, S., Etschmann, B., Mei, Y., Brugger, J., 2012a. An XAS study of speciation and thermodynamic properties of aqueous zinc bromide complexes at 25–150 °C. Chemical Geology 298–299, 57–69.

Liu, W., Migdisov, A., Williams-Jones, A., 2012b. The stability of aqueous nickel(II) chloride complexes in hydrothermal solutions: Results of UV-Visible spectroscopic experiments. Geochimica et Cosmochimica Acta 94, 276–290.
Lüdemann, H.D., Franck, E.U., 1967. Absorptionsspektren bei hohen drucken und temperaturen. I: wäßrige Co(II)- und Ni(II)-halogenid-lösungen bis zu 500 °C und 6 kbar. Berichte der Bunsen-Gesellschaft für Physikalische Chemie 71, 455–460.
Lüdemann, H.D., Franck, E.U., 1968. Absorptionsspektren bei hohen drucken und temperaturen. II [1] kobalt(II)- und nickel(II)-halogenide in konzentrierten alkalihalogenid-lösungen. Bunsen-Gesellschaft für Physikalische Chemie 72, 514–523.
Mayanovic, R.A., Anderson, A.J., Bassett, W.A., Chou, I., 1999. XAFS measurements on zinc chloride aqueous solutions from ambient to supercritical conditions using the diamond anvil cell. Journal of Synchrotron Radiation 6, 195–197.
Merkling, P.J., Muñoz-Páez, A., Sánchez Marcos, E., 2002. Exploring the capabilities of X-ray absorption spectroscopy for determining the structure of electrolyte solutions: computed spectra for Cr^{3+} or Rh^{3+} in water based on molecular dynamics. Journal of the American Chemical Society 124, 10911–10920.
Migdisov, A.A., Zezin, D., Williams-Jones, A.E., 2011. An experimental study of cobalt (II) complexation in Cl- and H_2S-bearing hydrothermal solutions. Geochimica et Cosmochimica Acta 75, 4065–4079.
Molnar, F., Watkinson, D.H., Jones, P.C., 2001. Multiple hydrothermal processes in footwall units of the North Range, Sudbury Igneous Complex, Canada, and implications for the genesis of vein-type Cu–Ni–PGE deposits. Economic Geology 96, 1645–1670.
Palmer, D.A., Bénézeth, P., Xiao, C.B., Wesolowski, D.J., Anovitz, L.M., 2011. Solubility measurements of crystalline NiO in aqueous solution as a function of temperature and pH. Journal of Solution Chemistry 40, 680–702.
Parise, J., 1980. Structure of hazelwoodite (Ni_3S_2). Acta Crystallographica Section B: Structural Science 36, 1179–1180.
Parr, R.G., Yang, W., 1989. Density-Functional Theory of Atoms and Molecules, 16. Oxford University Press, USA, New York.
Perdew, J.P., Burke, K., Ernzerhof, M., 1996. Generalized gradient approximation made simple. Physical Review Letters 77, 3865–3868.
Pertlik, F., 1986. Structures of hydrothermally synthesized cobalt(II) carbonate and nickel(II) carbonate. Acta Crystallographica Section C: Crystal Structure Communications 42, 4–5.
Pye, C.C., Ziegler, T., 1999. An implementation of the conductor-like screening model of solvation within the Amsterdam density functional package. Theoretical Chemistry Accounts 101, 396–408.
Ravel, B., Newville, M., 2005. ATHENA, ARTEMIS, HEPHAESTUS: data analysis for X-ray absorption spectroscopy using IFEFFIT. Journal of Synchrotron Radiation 12, 537–541.
Ripley, E.M., Sarkar, A., Li, C., 2005. Mineralogic and stable isotope studies of hydrothermal alteration at the Jinchuan Ni–Cu deposit, China. Economic Geology 100, 1349–1361.
Rousseau, B., Maes, S.T., Lenstra, A.T.H., 2000. Systematic intensity errors and model imperfection as the consequence of spectral truncation. Acta Crystallographica Section A: Foundations 56, 300–307.
Ryzhenko, B.N., Bryzgalin, O.V., Artamkina, I.Y., Spasennykh, M.Y., Shapkin, A.I., 1985. An electrostatic model for the electrolytic dissociation of inorganic substances dissolved in water. Geochemistry International 22, 138–144.
Sasaki, S., Fujino, K., Takeuchi, Y., 1979. X-ray determination of electrondensity distributions in oxides, MgO, MnO, CoO, and NiO, and atomic scattering factors of their constituent atoms. Proceedings of the Japan Academy. Series B 55, 43–48.
Seward, T.M., Barnes, H.L., 1997. Metal transport by hydrothermal ore fluids. In: Barnes, H.L. (Ed.), Geochemistry of Hydrothermal Ore Deposits. Wiley, New York, pp. 435–486.
Seward, T.M., Driesner, T., 2004. Hydrothermal solution structure: experiments and computer simulations. In: Palmer, D.A., Fernández-Prini, R., Harvery, A.H. (Eds.), Aqueous Systems at Elevated Temperatures and Pressure. Elsevier Academic Press, pp. 149–182.
Shulman, G.R., Yafet, Y., Eisenberger, P., Blumberg, W.E., 1976. Observations and interpretation of X-ray absorption edges in iron compounds and proteins. Proceedings of the National Academy of Sciences of the United States of America 73, 1384–1388.
Shvarov, Y.V., Bastrakov, E.N., 1999. HCh, a software package for geochemical equilibrium modeling: user's guide. Australian Geological Survey Organisation (Record 1999/25).
Shvarov, Y.V., 2008. HCh: new potentialities for the thermodynamic simulation of geochemical systems offered by windows. Geochemistry International 46, 834–839.
Simonet, V., Calzavara, Y., Hazemann, J.L., Argoud, R., Geaymond, O., Raoux, D., 2002. Structure of aqueous $ZnBr_2$ solution probed by X-ray absorption spectroscopy in normal and hydrothermal conditions. Journal of Chemical Physics 116, 2997–3006.
Suh, I.-K., Ohta, H., Waseda, Y., 1988. High-temperature thermal expansion of six metallic elements measured by dilatation method and X-ray diffraction. Journal of Materials Science 23, 757–760.
Suleimenov, O.M., 2004. Simple, compact, flow-through, high temperature high pressure cell for UV-Vis spectrophotometry. The Review of Scientific Instruments 75, 3363–3364.
Susak, N.J., Crerar, D.A., 1985. Spectra and coordination changes of transition metals in hydrothermal solutions: implications for ore genesis. Geochimica et Cosmochimica Acta 49, 555–564.
Sverjensky, D.A., Shock, E.L., Helgeson, H.C., 1997. Prediction of the thermodynamic properties of aqueous metal complexes to 1000 °C and 5 kb. Geochimica et Cosmochimica Acta 61, 1359–1412.
Tagirov, B.R., Zotov, A.V., Akinfiev, N.N., 1997. Experimental study of dissociation of HCl from 350 to 500°C and from 500 to 2500 bars: thermodynamic properties of HCl(aq). Geochimica et Cosmochimica Acta 61, 4267–4280.
te Velde, G., et al., 2001. Chemistry with ADF. Journal of Computational Chemistry 22, 931–967.
Tenailleau, C., Etschmann, B., Ibberson, R.M., Pring, A., 2006. A neutron powder diffraction study of Fe and Ni distributions in synthetic pentlandite and violarite using ^{60}Ni isotope. American Mineralogist 91, 1442–1447.
Testemale, D., Hazemann, J.L., Pokrovski, G.S., Joly, Y., Roux, J., Argoud, R., Geaymond, O., 2004. Structural and electronic evolution of the $As(OH)_3$ molecule in high temperature aqueous solutions: an X-ray absorption investigation. Journal of Chemical Physics 121, 8973–8982.
Testemale, D., Argoud, R., Geaymond, O., Hazemann, J.L., 2005. High pressure high temperature cell for X-ray absorption and scattering techniques. The Review of Scientific Instruments 76, 043905.
Testemale, D., Brugger, J., Liu, W., Etschmann, B., Hazemann, J.-L., 2009. In-situ X-ray absorption study of iron(II) speciation in brines up to supercritical conditions. Chemical Geology 264, 295–310.
Tian, Y., Brugger, J., Liu, W., Borg, S., Etschmann, B., O'Neill, B., Testemale, D., Hazemann, J.-L., Glover, C., Ngothai, Y., Jung, M., Peak, J., 2010. High-Temperature and Pressure Spectroscopic Cell for *In-Situ* XAS Study of Supercritical Fluids at the Australian Synchrotron, Chemeca 2010, Adelaide, S. A., Australia.
Tremaine, P.R., Leblanc, J.C., 1980. The solubility of nickel oxide and hydrolysis of Ni^{2+} in water to 573 K. The Journal of Chemical Thermodynamics 12, 521–538.
Uchida, E., Goryozono, Y., Naito, M., 1996. Aqueous speciation of magnesium, strontium, nickel and cobalt chlorides in hydrothermal solutions at 600 °C and 1 kbar. Geochemical Journal 30, 99–109.
Vaughan, D.J., Craig, J.R., 1985. The crystal chemistry of iron–nickel thiospinels. American Mineralogist 70, 1036–1043.
Vinokurov, I.A., Kankare, J., 1998. Beer's law and the isosbestic points in the absorption spectra of conductive polymers. The Journal of Physical Chemistry. B 102, 1136–1140.
Vosko, S.H., Wilk, L., Nusair, M., 1980. Accurate spin-dependent electron liquid correlation energies for local spin density calculations: a critical analysis. Canadian Journal of Physics 58, 1200–1211.
Wagner, T., Lorenz, J., 2002. Mineralogy of complex Co–Ni–Bi vein mineralisation, Bieber deposit, Spessart, Germany. Mineralogical Magazine 66, 385–407.
Wallen, S.L., Palmer, B.J., Fulton, J.L., 1998. The ion pairing and hydration structure of Ni^{2+} in supercritical water at 425 °C determined by X-ray absorption fine structure and molecular dynamics studies. Journal of Chemical Physics 108, 4039–4046.
Westre, T.E., Kennepohl, P., DeWitt, J.G., Hedman, B., Hodgson, K.O., Solomon, E.I., 1997. A multiplet analysis of Fe *K*-edge $1s \rightarrow 3d$ pre-edge features of iron complexes. Journal of the American Chemical Society 119, 6297–6314.
Yamamoto, T., 2008. Assignment of pre-edge peaks in *K*-edge X-ray absorption spectra of 3d transition metal compounds: electric dipole or quadrupole? X-Ray Spectrometry 37, 572–584.
Ziemniak, S.E., Goyette, M.A., 2004. Nickel(II) Oxide Solubility and Phase Stability in High Temperature Aqueous Solutions. Journal of Solution Chemistry 33, 1135–1159.